CWP-618
September 2008

Range and resolution analysis of wide azimuth angle decomposition

Gabriela Melo

— Master's Thesis —
Geophysics

Defended on September 19, 2008

Advisor: Paul Sava

Center for Wave Phenomena
Colorado School of Mines
Golden, Colorado 80401
(1) 303 273-3557

Abstract

Imaging in complex media benefits from uniform illumination of the target from all possible directions. Moreover, it is desirable to recover reflectivity from seismic data as a function of incidence and azimuthal angles at every location over the reflector. Applications of angle-dependent reflectivity include velocity and anisotropy estimation and amplitude versus angle (AVA) analysis. One way of constructing angle-dependent reflectivity is to apply an extended imaging condition to the extrapolated source and receiver wavefields. This imaging condition allows one to construct images as a function not only of three-dimensional position but also space lags of the source/receiver wavefield cross-correlation. The information in the space-lag domain can be mapped into the angle domain defined by the reflection and azimuthal angles at every image point. The relationship between sampling parameters in the angle and space-lag domain, together with the equations used to perform the mapping, show that the sample interval in the space-lag domain controls the range of angles that can be accurately recovered from the image in this domain. This is the range of angles for which the energy is well focused, at the depth of the reflector, in the angle-domain common-image gathers. From the amplitude spectrum of the lag-domain common-image gathers, we can calculate the maximum angle that limits this range. For angles greater than this upper bound, the image energy starts to spread away from the depth of the reflector. We also show that the range of space-lags influences the sample interval in the angle domain. This analysis is important for the case where the angle-domain common-image gathers are employed for amplitude versus angle analysis. In this case, the amplitudes corresponding to the angles outside of this range would not be reliable, regardless of how accurate wavefield reconstruction is.

Table of Contents

Chapter 1 Introduction **1**

Chapter 2 Angle decomposition methods **5**

2.1 The wide-azimuth angle decomposition equations of Sava & Fomel (2005) 6
2.2 The wide-azimuth angle decomposition equations of Biondi & Tisserant (2004) 8
2.3 Equivalence of wide-azimuth angle decomposition methods 12

Chapter 3 Resolution and range analysis of angle-domain common-image gathers **15**

3.1 2D range and resolution analysis 15
3.2 3D range and resolution analysis 26

Chapter 4 Synthetic examples **39**

4.1 Depth dependent velocity $v(z)$ and/or dipping reflectors 39
4.2 SEG/EAGE salt dome model 45

Chapter 5 Conclusions **53**

References **55**

Appendix A Angle decomposition equations **57**

Chapter 1

Introduction

Many hydrocarbon reservoirs are embedded in complex media characterized by strong velocity heterogeneity and discontinuities associated with salt bodies. In the presence of complex subsurface structures, it is crucial to form a reflector map (image) with well focused energy for efficient development and exploration of reservoirs located in such areas. The right choice of procedures, from acquisition to data processing, is of fundamental importance since they all influence the image quality.

In order to produce accurate images it is necessary that the data contain enough information about the area of interest. Even with the use of the most sophisticated processing tools and techniques, it is impossible to achieve the desired image quality from narrow-azimuth data in complex media because these data do not contain all the necessary information needed to create good images.

In the wide-azimuth acquisition context there are two relevant parameters: the azimuth of the source/receiver line (surface azimuth) and the distance between source and receiver (surface offset). The surface azimuth is the angle of the line connecting source and receiver in relation to a reference direction on the acquisition surface. In wide-azimuth acquisition the surface azimuth varies over a wide range. For the remainder of the paper, data from wide-azimuth surveys are referred to as wide-azimuth data and data from narrow-azimuth surveys are referred to as narrow-azimuth data.

Data acquired at different surface azimuths illuminate different parts of the target. Varying the surface azimuth as well as the surface offset helps illuminating different parts of the target at different angles. In complex media, where velocity varies with position and may depend on direction of propagation, it is desirable to illuminate each location along the reflector from many directions in order to study how reflectivity changes with direction (at the image point). Some applications of wide-azimuth reflectivity are velocity analysis, amplitude versus angle analysis, and anisotropy estimation.

Salt bodies cause irregular illumination of targets located beneath them. This not only makes it difficult to properly image the shadow zones, but also creates spurious events in the images. Recently published work shows that it is possible to significantly improve image quality by acquiring and processing wide-azimuth data (Regone, 2006). The wide-azimuth data help to improve resolution in the velocity models (Michell *et al.*, 2006; LaDart *et al.*, 2006; Shoshitaishvili *et al.*, 2006), identify directional fractures and attenuate coherent noise (Shirui *et al.*, 2006), and consequently improve the image .

Here, the data are characterized by two surface parameters, namely, surface offset (source/receiver offset) and surface azimuth. In general, a reflection phenomenon can be characterized by two parameters as well: reflection angle and azimuthal angle at the image point (assuming the reflector dips are known). These angles are defined locally at the image point and, in general, are not simply related to the surface parameters, as explained next.

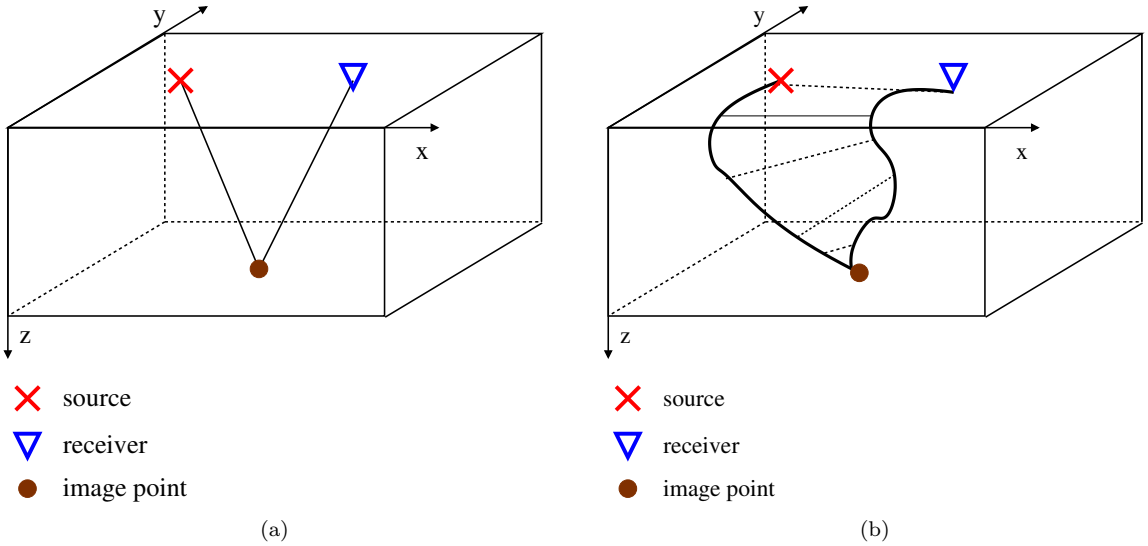

Figure 1.1. Schematic representations of ray paths in: simple homogeneous medium (a) and complex heterogeneous medium (b). In (a) the incident and reflected rays are straight lines whereas in (b) these rays deviate from these lines as a result of velocity variation.

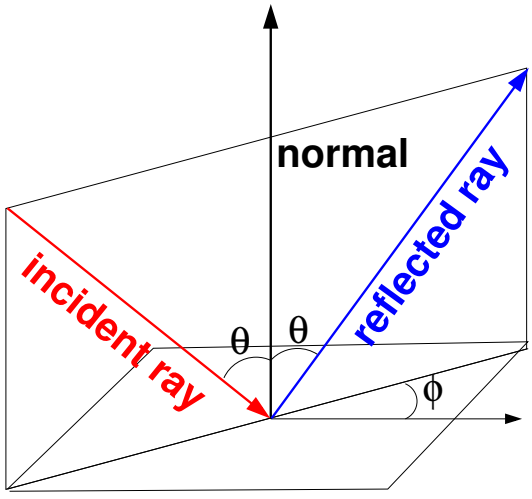

Figure 1.2. Geometrical relations between ray parameter vectors.

The reflection plane is the plane containing the incident ray from the source to the reflection point, the normal to this point, and the reflected ray from the reflection point to the receiver, all measured at the image point. This plane is defined in the vicinity of the image point. The angle between the incident/reflected ray and the normal is the reflection angle. The angle that characterizes the orientation of the reflection plane, in 3D, in relation to a chosen direction, is the azimuthal angle (Figure 1.2). When the subsurface is a homogeneous isotropic medium, the surface offset and azimuth are simply related to the reflection and azimuthal angles, respectively, at the reflection point, Figure 1.1(a), independent of the reflector dip. Changes in velocity cause the incident and reflected rays to deviate from straight lines to more complicated paths, Figure 1.1(b). Thus, when the medium is complex, the surface azimuth is not directly related to the azimuthal angle of the reflection plane at the image point, nor is the surface offset directly related to the reflection angle. Even though this relationship is indirect, a wide-azimuth acquisition is likely to increase the range of the azimuthal angles of the reflection planes at the image point.

To obtain accurate images in complex geology with large and sharp velocity variation, it is necessary to perform wavefield reconstruction (extrapolation) using methods capable of treating large lateral velocity variations and phenomena such as multipathing (Gray *et al.*, 2001). Wavefield extrapolation by downward-continuation methods (Gazdag & Sguazzero, 1985; Stoffa *et al.*, 1990; Freire & Stoffa, 1986; Kessinger, 1992; Cockshott & Jakubowicz, 1996), is one possible way to perform accurate wavefield reconstruction in such media, since it is capable to handle these issues. In this work, I use the Split Step Fourier downward-continuation method (Stoffa *et al.*, 1990).

Reflectivity information can be obtained by applying an imaging condition to the reconstructed source and receiver wavefields. One possible choice of imaging condition is a cross-correlation type imaging condition (Claerbout, 1971) that creates an image function of position in space. One possible way to construct angle-dependent reflectivity is through applying an extended imaging condition that preserves the orthogonal space lags from the source/receiver wavefield cross-correlation (Sava & Fomel, 2006) creating an image function of position in space and space lags. One can create space-lag-domain common-image gathers (lag gathers) from images obtained by extended imaging conditions, and then map the information in the lag domain to the angle domain, creating the so-called angle-domain common-image gathers (ADCIG or angle-gathers).

Migration velocity analysis (MVA), applied after migration by downward continuation, has often been performed using lag-domain common-image gathers (Biondi *et al.*, 2003; Biondi & Symes, 2004). These gathers are usually referred to as offset-domain common-image gathers (ODCIG). However, in this work, the term "space lag" is used to refer to the separation of the downward-continued wavefields at the image point while the word "offset" is reserved for the more traditional separation between source and receiver at the acquisition surface. Events in the lag gathers may suffer from ambiguity on the reflection position due to multipathing, which is a common phenomenon for propagation in complex media (Nolan & Symes, 1996). Reflector position ambiguity in the lag gathers, in turn, may lead to velocity update ambiguities. To alleviate this problem, the lag gathers can be transformed, as a function of the reflection angle at the image point, to angle gathers. Events in angle gathers uniquely represent energy scattered from specific locations in the subsurface. These events are uniquely associated with pairs of incident and reflected rays that, in turn, uniquely define the reflector (Prucha *et al.*, 1999; Stolk & Symes, 2002).

As indicated earlier, one way of constructing angle-dependent reflectivity is through

migration by wavefield extrapolation combined with an extended imaging condition. The space-lag images can be decomposed at every image point into components that depend on the reflection angle (Sava & Fomel, 2005, 2003; Mosher & Foster, 2000; Prucha *et al.*, 1999). It is also possible to construct angle-dependent reflectivity by integral methods (Xu *et al.*, 1998; Brandsberg-Dahl *et al.*, 1999; Bleistein *et al.*, 2005). For wide-azimuth data, it is possible to decompose the space lags in reflection and azimuthal angle (Sava & Fomel, 2003; Biondi & Tisserant, 2004; Sava & Fomel, 2005).

The goal of this work is to understand the relationship between the sample parameters in both space-lag and angle domain and to establish the implications in the angle domain of choices of sample parameters in the space-lag domain. Then, it is possible to choose the wanted sampling parameters for required to implement the extended imaging condition.

In Chapter 2, I construct angle-dependent reflectivity by performing angle decomposition based on the geometry of ray vectors at the image point (Sava & Fomel, 2005). Also, I review the Biondi & Tisserant (2004)'s decomposition method and show that it is equivalent to the method I use and also present in Chapter 2.

In Chapter 3, I study the relationship between the sample parameters in both space-lag and angle domain. I obtain a reciprocal resolution/range relationship between lag and angle domain from the equations used to perform the lag to angle-domain mapping, together with the sampling parameters in both domains. First, this relationship shows that the resolution in the angle domain (which is associated with the sample interval parameter) is controlled by the range (which is associated with the number of samples times the sample interval) in the space-lag domain. Secondly, this relationship shows that the sample interval in the space-lag domain controls the range of angles that can be accurately recovered from the image in the space-lag domain. I perform the analysis for two-dimensional (2D) and wide-azimuth three-dimensional (3D) geometries. In 2D, there is a limited range of reflection angles for which the energy focuses, at the depth of the reflector, in the angle gathers; for angles outside this range, the energy starts to spread. In 3D, this range varies with the azimuthal angle. Using these relationships, one can choose the parameters in both domains according to the desired resolution and range on angles for the ADCIGs. Synthetic examples are presented to illustrate the sampling relationship between space-lag and angle domain as well as an example of the angle decomposition.

In Chapter 4 I present synthetic numerical examples. The first example is a simple homogeneous model with a flat reflector and is meant to show the differences between reflections inside and outside the range of angles mentioned discussed in Chapter 3. I create two scenarios with different velocity models and construct nine CIGs for the same locations in both cases. In the first case, the reflections occur for angles that are inside the range mentioned above and, in the second case, the reflections occur at larger angles. Observing the angle gathers for these two situations we can see the difference in the energy focus is for these two cases. The second example demonstrates the analysis from Chapter 3 in a more complex situation where I use the SEG/EAGE salt dome model to create the data and the images. In this example, I show only one CIG containing many reflections, where some of them are inside and some are outside the range of accurately recoverd angles.

Chapter 2

Angle decomposition methods

I begin this chapter by deriving the angle-decomposition equations I use in this work. These equations are based on the geometric relationships of the ray parameter vectors described in Sava & Fomel (2005). Then, I review the angle-decomposition method of Biondi & Tisserant (2004). Finally, I compare the two methods to show that they are equivalent. In this work, I use the equations based on Sava & Fomel (2005) work because they have a more intuitive and simple geometrical interpretation.

Migration of seismic data consists mainly of two parts: a wavefield reconstruction procedure that creates a source wavefield U_s and a receiver (scattered) wavefield U_r, at all space locations and all times (or frequencies) given a presumed velocity field; an imaging condition that extracts an image I (reflectivity information) from the reconstructed source and receiver wavefields, U_s and U_r.

One can extract an image (I) from the reconstructed source and receiver wavefields by applying a conventional correlation imaging condition (Claerbout, 1971),

$$I(\boldsymbol{x}) = \sum_{\omega} U_r(\boldsymbol{x},\omega) U_s^*(\boldsymbol{x},\omega) \;, \tag{2.1}$$

where $\boldsymbol{x} = (x, y, z)$ are the space coordinates, ω is the temporal frequency, $U_s^*(\boldsymbol{x},\omega)$ is the complex conjugate of the source wavefield, $U_r(\boldsymbol{x},\omega)$ is the receiver wavefield, and $I(\boldsymbol{x})$ is the image, which depends on the particular choice of source and receiver configurations. This image contains information for velocity analysis, such as the presence of non-focused diffracted energy at the supposed reflection positions. It is possible, however, to obtain additional velocity information by applying a more general imaging condition, sometimes referred to as the extended imaging condition (Sava & Fomel, 2005).

One can define an extended imaging condition by space and time cross-correlation that retains the space and/or time lags. Here, I employ this extended imaging condition to obtain an image function of the space coordinates and space lags,

$$I(\boldsymbol{x},\boldsymbol{\lambda}) = \sum_{\omega} U_r(\boldsymbol{x}+\boldsymbol{\lambda},\omega) U_s^*(\boldsymbol{x}-\boldsymbol{\lambda},\omega) \;. \tag{2.2}$$

Here, $\boldsymbol{\lambda} = (\lambda_x, \lambda_y, \lambda_z)$ are the cross-correlation space lags. The image $I(\boldsymbol{x},\boldsymbol{\lambda})$ contains information for velocity analysis aimed at improving the presumed velocity model. When the velocity model used for migration is wrong, the energy does not map completely to the zero-lag image, so it is possible to obtain velocity information by looking at the energy in the image $I(\boldsymbol{x},\boldsymbol{\lambda})$ for the other lags different from zero. The conventional image $I(\boldsymbol{x})$ from equation 2.1 is equivalent to the extended image $I(\boldsymbol{x},\boldsymbol{\lambda})$ at $\boldsymbol{\lambda} = \mathbf{0}$.

An image function of space, reflection angle θ, and azimuthal angle ϕ can be obtained by mapping the information from the lag domain into the angle domain (Sava

& Fomel, 2005)

$$I(\boldsymbol{x}, \boldsymbol{\lambda}) \longrightarrow I(\boldsymbol{x}, \theta, \phi) \; . \tag{2.3}$$

The angle between the incident or reflected ray and the reflector normal (at the image point) is the reflection angle, θ. The angle that characterizes the orientation of the reflection plane in 3D, in relation to a specified direction, is the azimuthal angle, ϕ. As mentioned earlier, these angles are related to a local geometry of source and receiver ray vectors at the image point.

2.1 The wide-azimuth angle decomposition equations of Sava & Fomel (2005)

The relationship between the space lags $\boldsymbol{\lambda}$, and the reflection and azimuthal angles, θ and ϕ, in general, involves (k_x, k_y, k_z), the wavenumbers related to the space coordinates (x, y, z), and $(k_{\lambda_x}, k_{\lambda_y}, k_{\lambda_z})$, the wavenumbers related to the space lags $(\lambda_x, \lambda_y, \lambda_z)$ (equations A.14 and A.18). It is possible to avoid the vertical space lag λ_z by taking advantage of the fact that the wavenumber vectors $\boldsymbol{k_x}$ and $\boldsymbol{k_\lambda}$ are orthogonal (equations A.19 and A.20). This observation allows one to reduce the image $I(\boldsymbol{x}, \boldsymbol{\lambda})$ from six to five dimensions. The mapping equations used in this work are,

$$\tan\theta = \frac{\sqrt{(k_{\lambda_x}^2 + k_{\lambda_y}^2)k_z^2 + (-k_x k_{\lambda_x} - k_y k_{\lambda_y})^2}}{\sqrt{k_z^2(k_x^2 + k_y^2 + k_z^2)}} \; , \tag{2.4}$$

and

$$\cos\phi = \frac{k_z^2 k_{\lambda_y} + k_x k_y k_{\lambda_x} + k_y^2 k_{\lambda_y}}{\sqrt{(k_{\lambda_y}(k_z^2 + k_y^2) + k_x k_y k_{\lambda_x})^2 + (-k_{\lambda_x}(k_x^2 + k_z^2) - k_y k_x k_{\lambda_y})^2}} \; . \tag{2.5}$$

These equations are derived in the Appendix.

Implementation of equations 2.4 and 2.5 seemingly requires a five-dimensional Fourier transform to create ADCIGs, functions of angles θ and ϕ, for all locations over the reflector. This transformation would involve a great α_x and α_y computational effort and storage of a five-dimensional hypercube $I(x, y, z, \theta, \phi)$, which might not be feasible in practice. Thus, the ADCIGs are created just for certain locations over the reflector, i.e., for only some x and y locations. When constructing the ADCIGs at only selected horizontal positions, one cannot apply the Fourier transform over the horizontal surface coordinates x and y, so one cannot construct images functions of space wavenumbers k_x and k_y. It is possible to get around this limitation by considering the local slopes measured on the image at every location in space.

Letting α_x and α_y denote the local reflector dip along the x and y directions, respectively, and observing that

$$\alpha_x = \frac{\partial z}{\partial x} = \frac{k_x}{k_z} \; , \tag{2.6}$$

and

$$\alpha_y = \frac{\partial z}{\partial y} = \frac{k_y}{k_z} \; . \tag{2.7}$$

I use these relationships in equations 2.6 and 2.7 for $\tan\theta$ and $\cos\phi$, respectively, to

obtain

$$\tan\theta = \frac{\sqrt{k_{\lambda_x}^2(1+\alpha_x^2)+k_{\lambda_y}^2(1+\alpha_y^2)+2k_{\lambda_x}k_{\lambda_y}\alpha_x\alpha_y}}{\sqrt{k_z^2(\alpha_x^2+\alpha_y^2+1)}}\,, \tag{2.8}$$

and

$$\cos\phi = \frac{k_{\lambda_y}(1+\alpha_y^2)+\alpha_x\alpha_y k_{\lambda_x}}{\sqrt{(k_{\lambda_y}(1+\alpha_y^2)+\alpha_x\alpha_y k_{\lambda_x})^2+(k_{\lambda_x}(1+\alpha_x^2)+\alpha_x\alpha_y k_{\lambda_y})^2}}\,. \tag{2.9}$$

In this manner, it is possible to eliminate k_x and k_y from equations 2.4 and 2.5. This reduces the size of FFTs from five to three dimensions, reduces the amount of data to be stored, and makes computations independent for each CIG location as I will show bellow.

The input data for creating a CIG are the hypercube image $I(\boldsymbol{x},\boldsymbol{\lambda})$ and the local slopes in the x and y direction, α_x and α_y, respectively. Construction of one CIG by applying the angle decomposition described by relations 2.8 and 2.9 involves the following steps:

- **select the horizontal CIG location (x_0, y_0) and obtain the lag-domain CIG $I(z,\lambda_x,\lambda_y) = I(x=x_0, y=y_0, z, \lambda_x, \lambda_y, \lambda_z=0)$ from the image $I(\boldsymbol{x},\boldsymbol{\lambda})$;**
- **apply a three-dimensional Fourier transform on axes z, λ_x, λ_y**

$$I(z,\lambda_x,\lambda_y) \rightarrow I(k_z,k_{\lambda_x},k_{\lambda_y})\,;$$

- **loop over k_z;**
- **loop over ϕ;**
- **loop over θ;**
- **calculate k_{λ_x} and k_{λ_y} from relations 2.8 and 2.9;**
- **perform the mapping**

$$I(k_z,k_{\lambda_x},k_{\lambda_y}) \rightarrow I(k_z,\theta,\phi)$$

  according to relations 2.8 and 2.9;

- **apply a one-dimensional inverse Fourier transform for the depth axis**

$$I(k_z,\theta,\phi) \rightarrow I(z,\theta,\phi)\,,$$

  to obtain the angle domain CIG.

As discussed previously in this section, the fact that this algorithm takes the local slopes α_x and α_y as given parameters allows us to create CIGs in chosen horizontal locations independently of each other. For each location it is necessary to store a 3-dimensional image. This algorithm ("pull" implementation) loops over the output, θ and ϕ, and pulls information from the input, k_{λ_x} and k_{λ_y}. The step that corresponds to the mapping, $I(z,\lambda_x,\lambda_y) \rightarrow I(k_z,k_{\lambda_x},k_{\lambda_y})$, involves an interpolation step because the values of k_{λ_x} and k_{λ_y} obtained from θ and ϕ are not necessarily uniformly sampled. An alternative option ("push" implementation) loops over the input domain and pushes information into the output. In this way k_{λ_x} and k_{λ_y} are used to calculate θ and ϕ. In this

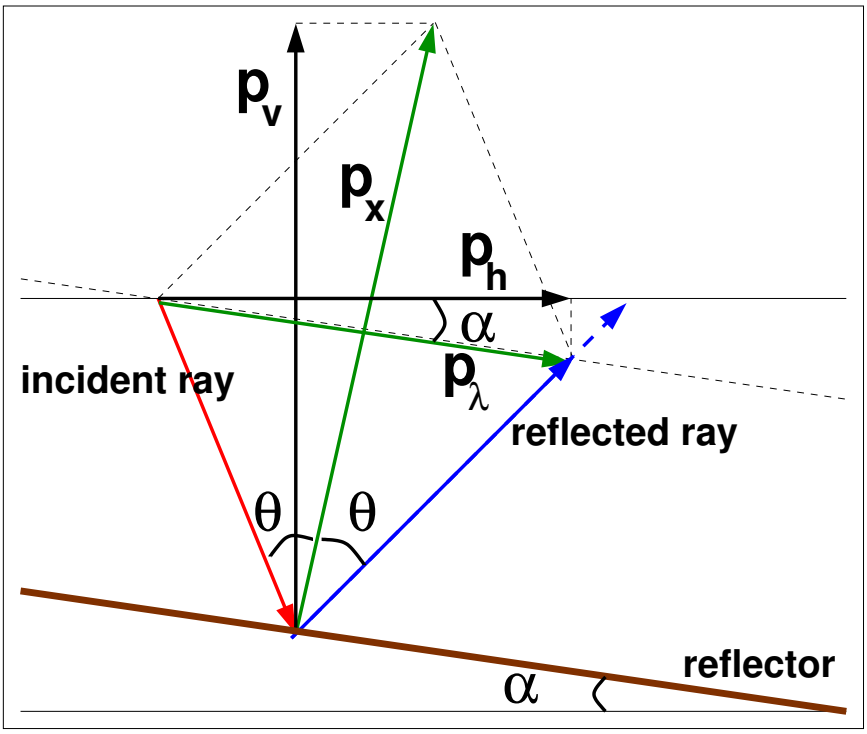

Figure 2.1. 2D geometrical relationships between ray parameter vectors. The vectors p_x and p_λ are the wavenumbers relative to x and λ, respectively, p_h is the horizontal component of p_λ, p_v is the vertical component of p_x, α is the reflector dip, and θ is the reflection angle.

thesis, I use nearest neighbor interpolation that can be easily implemented using both approaches. However, in more accurate or general interpolations it is more convenient to interpolate using uniformly sampled data to obtain data in between samples than to use non-uniformly sampled data to create sampled data. For this reason, I choose to use the pull version.

The computer effort that it takes to create a CIG for one horizontal location is of the order $n_{k_z} n_\theta n_\phi$, corresponding to the three loops, where n_{k_z}, n_θ and n_ϕ are the number of samples in the k_z, θ and ϕ dimensions, respectively.

2.2 The wide-azimuth angle decomposition equations of Biondi & Tisserant (2004)

In this section, I describe the wide-azimuth decomposition of Biondi & Tisserant (2004). They first derive their decomposition in 2D, then use their 2D formulation in common-azimuth slices on the acquisition surface in 3D and finally generalize their method to 3D."

Figure 2.1 shows the geometry for the 2D case. In this figure we see a line representing the reflector dipping by an angle α. The ray parameter vectors in this figure

are

$$\boldsymbol{p_x} = \frac{\boldsymbol{k_x}}{\omega} , \tag{2.10}$$

$$\boldsymbol{p_\lambda} = \frac{\boldsymbol{k_\lambda}}{\omega} , \tag{2.11}$$

$$\boldsymbol{p_v} = |\boldsymbol{p_x}| \cos\alpha , \tag{2.12}$$

$$\boldsymbol{p_h} = |\boldsymbol{p_\lambda}| \cos\alpha . \tag{2.13}$$

According to A.11, $\boldsymbol{p_x}$ is orthogonal to the reflector. The reflection angle θ is given by

$$\begin{aligned} |\tan\theta| &= \frac{|\boldsymbol{p_\lambda}|}{|\boldsymbol{p_x}|} \\ &= \frac{|\boldsymbol{p_h}|/\cos\alpha}{|\boldsymbol{p_v}|/\cos\alpha} \\ &= \frac{|\boldsymbol{p_h}|}{|\boldsymbol{p_v}|} \\ &= \frac{|p_{\lambda_x}|}{|p_z|} \\ &= \frac{|k_{\lambda_x}|}{|k_z|} . \end{aligned} \tag{2.14}$$

Next, I examine the common-azimuth situation, where the incident and reflected rays are contained tilted by an angle δ around the x-axis, i.e., the reflection plane is not necessarily vertical but its azimuthal angle is the same as the source/receiver surface azimuth. Consider the same plane as in Figure 2.1, in 3D, rotated by an angle δ around the y direction, as shown in Figure 2.2. That way, the propagation is contained in a tilted plane where the vertical axis is k'_z (assuming the medium is homogeneous). Changing variables from z to z' leads to

$$\frac{dz'}{dz} = \cos\delta \quad \Rightarrow \quad \cos\delta = \frac{1}{\sqrt{1+\dfrac{k_y^2}{k_z^2}}} , \tag{2.15}$$

and now it is possible to express θ as a function of the new z' axis:

$$\begin{aligned} |\tan\theta| &= \frac{|k_{\lambda_x}|}{|k'_z|} \\ &= \frac{|k_{\lambda_x}|}{|k_z|}\cos\delta \\ &= \frac{|k_{\lambda_x}|}{|k_z|}\frac{1}{\sqrt{1+\dfrac{k_y^2}{k_z^2}}} . \end{aligned} \tag{2.16}$$

Now the problem is extended to the case where the azimuthal angle of the reflection plane is different from the surface azimuth. In general, the incident/reflected rays and the reflector normal are not coplanar along the entire ray path due to lateral changes

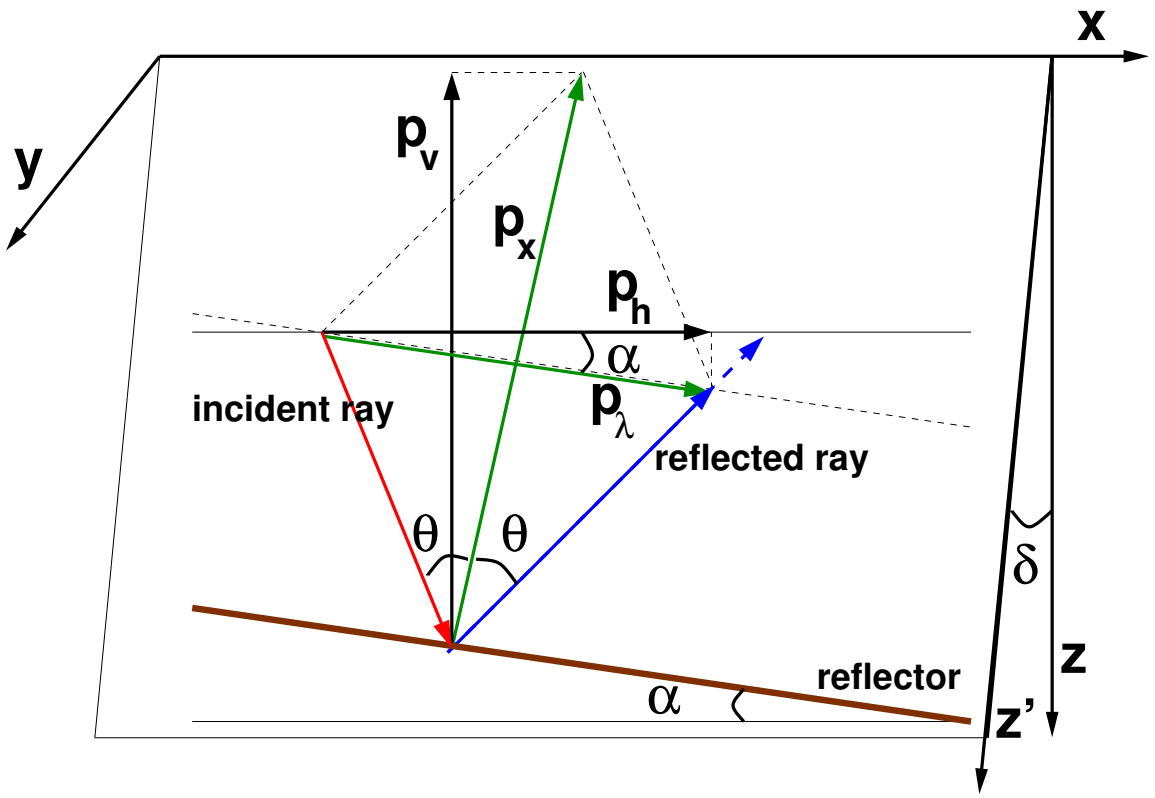

Figure 2.2. Common-azimuth geometrical relationships between ray parameter vectors. The vectors p_x and p_λ are the wavenumbers relative to x and λ, respectively, p_h is the horizontal component of p_λ, p_v is the vertical component of p_x, α is the reflector dip, θ is the reflection angle, and δ is the reflection dip around axis y.

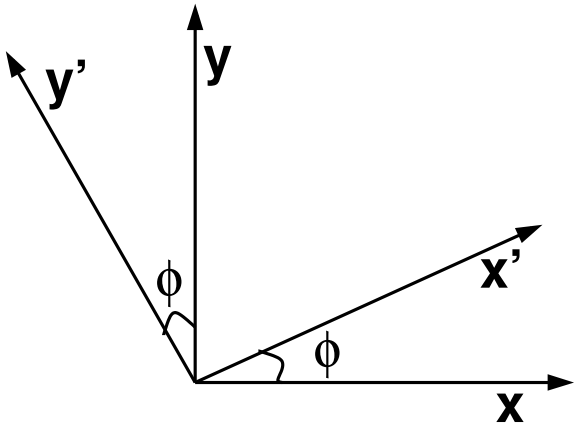

Figure 2.3. rotated coordinate system obtained after rotating the original coordinate system by an angle ϕ

in the velocity that cause ray bending. However, if the migration velocity is correct, the incident/reflected rays and the normal are coplanar at the reflection point. This way, the coplanarity condition (Biondi & Palacharla, 1996)

$$k_{\lambda_y} = \frac{k_y k_x k_{\lambda_x}}{k_z^2 + k_y^2} \ , \tag{2.17}$$

can be used at the reflection point.

If ϕ is the azimuthal angle of the reflection plane in the original coordinate system, in relation to the in-line direction, then a rotation of the $x-y$ plane by an angle ϕ, around the z-axis, will reduce the general 3D case to the common-azimuth case. This way, the azimuthal angle is zero and the line that intersects the horizontal plane is parallel to the in-line direction in the rotated coordinate system. In the rotated coordinate system, the space wavenumbers are

$$k_x^{'} = k_x \cos\phi - k_y \sin\phi \ , \tag{2.18}$$

$$k_y^{'} = k_x \sin\phi + k_y \cos\phi \ , \tag{2.19}$$

and the space-lag wavenumbers are

$$k_{\lambda_x}^{'} = k_{\lambda_x} \cos\phi - k_{\lambda_y} \sin\phi \ , \tag{2.20}$$

$$k^{'}{}_{\lambda_y} = k_{\lambda_x} \sin\phi + k_{\lambda_y} \cos\phi \ . \tag{2.21}$$

Thus, the 3D mapping equations are

$$k^{'}{}_{\lambda_y} = \frac{k_y^{'} k_x^{'} k_{\lambda_x}^{'}}{k_z^2 + k_y^{'2}} \tag{2.22}$$

and

$$\tan\theta = \frac{k_{\lambda_x}^{'}}{k_z} \frac{1}{\sqrt{1 + \dfrac{k_{\lambda_y}^{'2}}{k_z^2}}} \ . \tag{2.23}$$

As discussed in the previous section, implementation of equations 2.22 and 2.23 also appears to require a five-dimensional Fourier transform to create ADCIGs. To avoid a great computational effort and storage of a five-dimensional hypercube $I(x, y, z, \theta, \phi)$, ADCIGs are created just for certain locations over the reflector. Here, I use the local slopes measured on the image at every location in space, equations 2.6 and 2.7 as also discussed above. Since the mapping equations are written on the rotated system, the local slopes are also written in the rotated system as

$$a_x^{'} = \alpha_x \cos\phi - \alpha_y \sin\phi \ , \tag{2.24}$$

$$a_y^{'} = -\alpha_x \sin\phi + \alpha_y \cos\phi \ . \tag{2.25}$$

The mapping equations are rewritten as

$$k^{'}{}_{\lambda_y} = \frac{a_y^{'} a_x^{'} k_{\lambda_x}^{'}}{1 + a_y^{'2}} \tag{2.26}$$

and

$$\tan\theta = \frac{k^{'}_{\lambda_x}}{k_z}\frac{1}{\sqrt{1+a_y^{'2}}}\ . \tag{2.27}$$

The input data for creating a CIG are the hypercube image $I(\boldsymbol{x},\boldsymbol{\lambda})$ and the local slopes α_x and α_y in the x and y direction, respectively. Construction of one CIG by applying the angle decomposition described by relations 2.26 and 2.27 involves the following steps:

- **select the horizontal CIG location (x_0, y_0) and obtain the lag-domain CIG $I(z,\lambda_x,\lambda_y) = I(x=x_0, y=y_0, z, \lambda_x, \lambda_y, \lambda_z=0)$ from the image $I(\boldsymbol{x},\boldsymbol{\lambda})$;**
- **apply a three-dimensional Fourier Transform on axes z, λ_x, λ_y**

$$I(z,\lambda_x,\lambda_y) \rightarrow I(k_z, k_{\lambda_x}, k_{\lambda_y})\ ;$$

- **loop over k_z**
- **loop over ϕ**
- **loop over θ**
- **calculate $a^{'}_x$ and $a^{'}_y$ (local slopes on the rotated system)**
- **calculate $k^{'}_{\lambda_x}$ and $k^{'}{}_{\lambda_y}$ from relations 2.26 and 2.27, respectively**
- **calculate k_{λ_x} and k_{λ_y} by bringing $k^{'}_{\lambda_x}$ and $k^{'}{}_{\lambda_y}$ to the original coordinate system**
- **perform the mapping**

$$I(k_z, k_{\lambda_x}, k_{\lambda_y}) \rightarrow I(k_z, \theta, \phi)$$

- **apply a one-dimensional Inverse Fourier Transform on the depth axis**

$$I(k_z, \theta, \phi) \rightarrow I(z, \theta, \phi)$$

to obtain the angle-domain CIG.

This algorithm has the same pull structure as the algorithm presented in the previous section. The loops are the same and the cost of this algorithm is also of order $n_{k_z} n_\theta n_\phi$. Since the only difference between them are the mapping equations the two methods have the same basic characteristics, thus, the same computational effort.

2.3 Equivalence of wide-azimuth angle decomposition methods

Due to the different approaches in obtaining the angle decomposition equations from the two methods previously discussed, it may not be immediately evident that the methods are equivalent. According to the discussion in the previous sections, we see that the azimuthal reference used in both methods is the same: the in-line direction. Therefore, the azimuthal angle obtained from both methods is the same. While Biondi & Tisserant (2004) perform rotations on the coordinate system to calculate the angle θ, the previous method uses simple geometrical relationships between the ray parameter vectors in a stationary coordinate system.

One could simply argue that a rotation (or a sequence of rotations) of a coordinate system does not alter the length of vectors nor the angle between them. If R is a rotation matrix, then

$$|R\boldsymbol{x}|^2 = (R\boldsymbol{x})^T R\boldsymbol{x} = \boldsymbol{x}^T R^T R\boldsymbol{x} = \boldsymbol{x}^T\boldsymbol{x} = |\boldsymbol{x}|^2 \ . \tag{2.28}$$

Now, suppose R is the rotation matrix applied to the original coordinate system to transform it into the rotated system. Then,

$$\boldsymbol{p}'_{\boldsymbol{\lambda}} = R\boldsymbol{p}_{\boldsymbol{\lambda}} \ , \tag{2.29}$$

$$\boldsymbol{p}'_{\boldsymbol{x}} = R\boldsymbol{p}_{\boldsymbol{x}} \ , \tag{2.30}$$

where the vectors $\boldsymbol{p}'_{\boldsymbol{\lambda}}$ and $\boldsymbol{p}'_{\boldsymbol{x}}$ are the vectors $\boldsymbol{p}_{\boldsymbol{\lambda}}$ and $\boldsymbol{p}_{\boldsymbol{x}}$, respectively, in the rotated system. Therefore, we have

$$\frac{|\boldsymbol{p}'_{\boldsymbol{\lambda}}|}{|\boldsymbol{p}'_{\boldsymbol{x}}|} = \frac{|\boldsymbol{p}_{\boldsymbol{\lambda}}|}{|\boldsymbol{p}_{\boldsymbol{x}}|} = \tan\theta \ . \tag{2.31}$$

Numerical simulations confirm equivalence of the two methods used for construction of angle-domain common-image gathers.

As discussed before, both methods can be implemented by algorithms that have the same basic structure. They both take the same input, return the same output, and demand the same computational effort. If the azimuthal reference chosen is the in-line direction, there is really no substantial difference between them. However, I chose to use the method based on Sava & Fomel (2005)s' approach because it has a simpler and more straightforward geometrical interpretation not requiring rotations of the coordinate systems.

Chapter 3

Resolution and range analysis of angle-domain common-image gathers

Angle-domain common-image gathers are commonly used to perform migration velocity analysis (MVA) and amplitude versus angle analysis (AVA). Since the angle-domain common-image gathers are constructed from the space-lag-domain common-image gathers, it is important to understand the relationship between sampling in the angle and space-lag domains. This section is devoted to analyzing angle-domain resolution (sample interval) and range (bounds), as functions of the sampling parameters in the space-lag domain. The resolution study involves understanding how to choose the sampling parameters in the space-lag and angle domains such that the angle-domain be uniformly sampled and not aliased. The range analysis is meant to answer the question "What angle range can be accurately recovered for a given range and sampling in the lag-domain of migrated images obtained with an extended imaging condition?" By range I mean a limited (bounded) interval of angles that can be accurately recovered from the lag gathers. Once the relationships between angle and space-lag-domain sampling parameters are established, it is possible to control resolution and range in the angle domain by choosing the corresponding parameters in the space-lag domain. This analysis has implications for establishing the maximum angle range that could potentially be used for AVA and MVA.

3.1 2D range and resolution analysis

In 2D, the image obtained from the extended imaging condition is, in general, a function of four coordinates: $I = I(x, z, \lambda_x, \lambda_z)$. As discussed earlier, it is possible to use geometrical relationships between the wavenumber vectors to eliminate λ_z and reduce the necessary image size from four to three dimensions, i.e., $I = I(x, z, \lambda_x)$.

Given a space-lag common-image gather $I(z, \lambda_x)$ at location x, one can construct an angle-domain common-image gather using the mapping equation

$$\tan\theta = \frac{k_{\lambda_x}}{k_z} \ , \tag{3.1}$$

which requires the space-lag CIG to be transformed to the Fourier domain.

In discussing angle-domain resolution, I consider plesthe following model parameters: origin, sample interval, and number of sam on the depth axis, (o_z, d_z, n_z); on the space-lag axis, $(o_{\lambda_x}, d_{\lambda_x}, n_{\lambda_x})$; on the depth wavenumber axis, $(o_{k_z}, d_{k_z}, n_{k_z})$; and on the space-lag wavenumber axis, $(o_{k_{\lambda_x}}, d_{k_{\lambda_x}}, n_{k_{\lambda_x}})$.

Using conventional discrete Fourier transform theory, the sampling parameters, origin and sample interval of the wavenumbers k_z and k_{λ_x} can be expressed in terms of

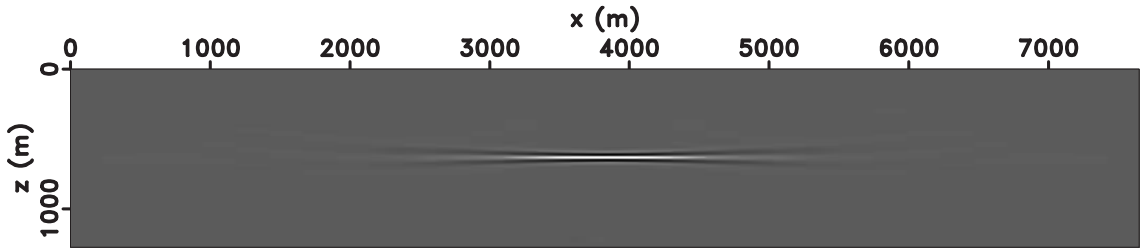

(a)

Figure 3.1. Migrated image $I(x,z)$: 2D flat reflector located at $z = 640$ m. The source is located at $z = 0$ and $x = 3840$ m.

the model parameters as

$$o_{k_z} = \frac{-1}{2d_z}, \quad d_{k_z} = \frac{1}{n_z d_z}\ , \tag{3.2}$$

and

$$o_{k_{\lambda_x}} = \frac{-1}{2d_{k_{\lambda_x}}}, \quad d_{k_{\lambda_x}} = \frac{1}{n_{\lambda_x} d_{\lambda_x}}\ . \tag{3.3}$$

The sampling parameters for the angle θ are origin, sample interval, and number of samples, $(o_\theta, d_\theta, n_\theta)$, One can analyze the behavior of d_θ as a function of k_{λ_x}, i.e., as a function of n_{λ_x} and d_{λ_x}. Using equation 3.1 and the relationships 3.3 and 3.2, one has $\theta = \theta(k_z, k_{\lambda_x}) = \theta(n_z, d_z, n_{\lambda_x} d_{\lambda_x})$. Isolating θ from equation 3.1,

$$\theta = \arctan \frac{k_{\lambda_x}}{k_z}\ , \tag{3.4}$$

by differentiating the above equation with respection to θ we obtain an expression for d_θ, namely,

$$d_\theta \quad = \quad \frac{k_z}{k_z^2 + k_{\lambda_x}^2} \frac{1}{n_{\lambda_x} d_{\lambda_x}}\ . \tag{3.5}$$

Noting that $n_{\lambda_x} d_{\lambda_x} = \lambda_{x_{max}}$, where $\lambda_{x_{max}}$ defines the range of the space-lag domain, we find

$$d_\theta = \frac{k_z}{k_z^2 + k_{\lambda_x}^2} \frac{1}{\lambda_{x_{max}}} \tag{3.6}$$

Thus, d_θ is inversely proportional to $n_{\lambda_x} d_{\lambda_x} = \lambda_{x_{max}}$. The parameter $\lambda_{x_{max}}$, which is the bound of the space-lag domain, controls the resolution (d_θ) in the angle domain: the larger the range in the space-lag domain, the better (smaller d_θ) the resolution in the angle domain.

To observe the influence of $\lambda_{x_{max}}$ on d_θ described by equation 3.6, I create an example where I construct angle gathers from lag gathers with different ranges $\lambda_{x_{max}}$.

Figure 3.1 is a migrated image that shows a horizontal reflector located at $z = 640$ m. The source is located on the center of the horizontal dimension, $x = 3840$ m.

Figure 3.2(a) is the lag-domain CIG constructed at the same horizontal location as the source, so, at this location the reflection corresponds to normal incidence. The lag

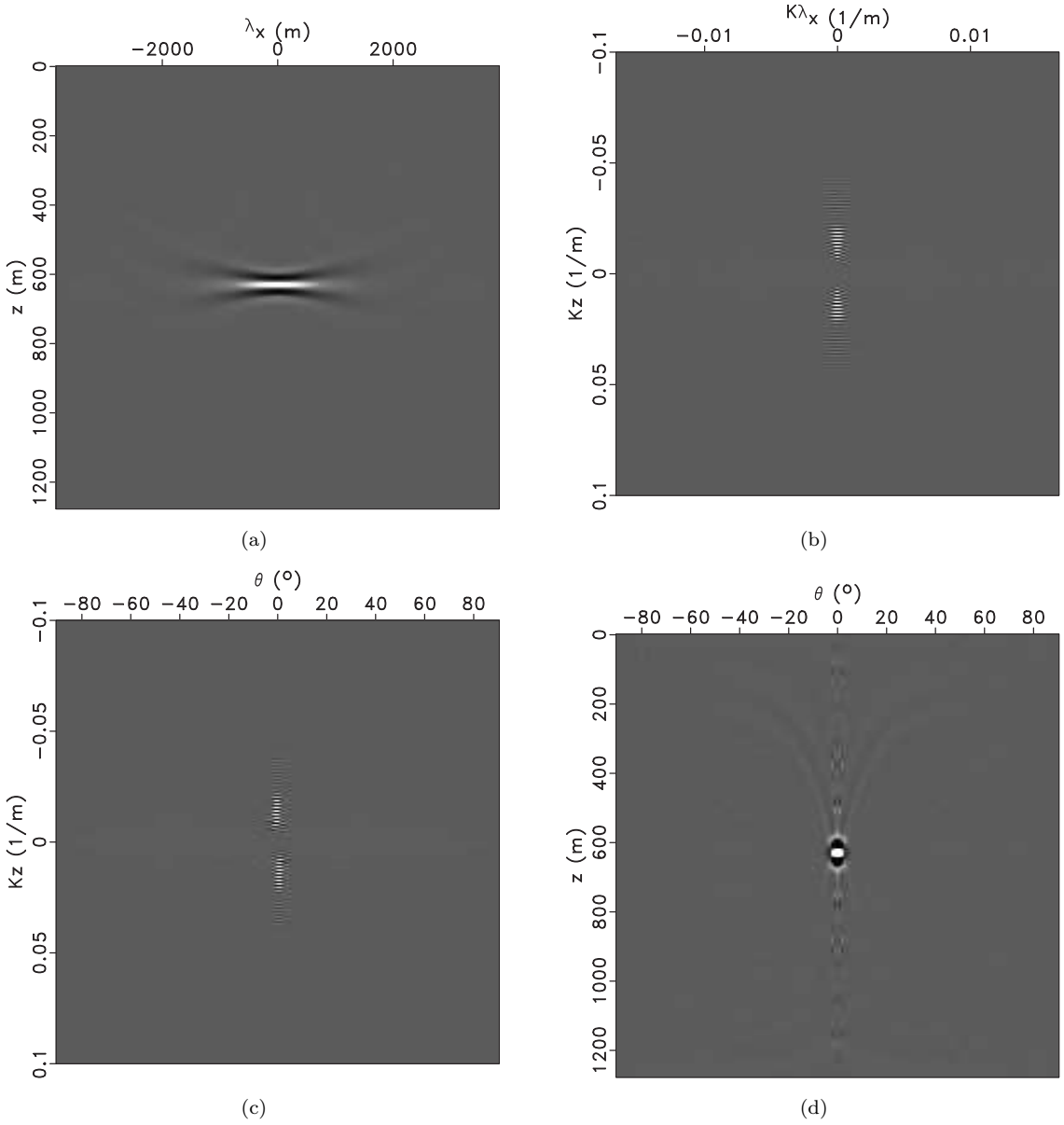

Figure 3.2. Construction of angle gather from lag gather for example of 2D flat reflector located at $z = 640$ m: (a) lag gather $I(z, \lambda_x)$; (b) lag gather in the Fourier domain $I(k_z, k_{\lambda_x})$; (c) mapping from k_{λ_x} to θ, $I(k_z, \theta)$; (d) angle-domain common-image gather $I(z, \theta)$.

dimension λ_x, in this case, covers the whole x dimension. The x dimension goes from 0 to 7680 m and since the lag dimension is centered at 0, it then goes from -3840 to 3840 m, i.e., $\lambda_{x_{max}} = 3840$ m. Figure 3.2(b) is the Fourier transform of the lag gather, and Figure 3.2(c) shows the image obtained after applying transformation 3.1 to the image in Figure 3.2(b). Figure 3.2(d) is the corresponding angle gather showing a reflection at $\theta = 0^\circ$, as expected.

Next, I create four different lag gathers where each one has $\lambda_{x_{max}}$ equal to half of the value of this parameter in the previous gather, Figures 3.3(a) – 3.3(d). Figures 3.4(a) – 3.4(d) are the angle gathers corresponding to the lag gathers in Figures 3.3(a) – 3.3(d). Observe that the smaller the range in the lag domain, the worse (larger d_θ) the resolution in the angle domain, as expected from equation 3.6.

According to equation 3.6, d_θ differs for each (k_z, k_{λ_x}), i.e., the angle domain is non-uniformly sampled. For processing reasons, one would like to have the angle domain uniformly sampled. One possible way to achieve that is to sample the angle domain uniformly using a d_θ chosen such as to avoid aliasing. The minimum value of d_θ, in order to avoid aliasing, is

$$d_{\theta_{min}} = \frac{k_{z_{max}}}{k_{z_{max}}^2 + k_{\lambda_{x_{max}}}^2} \frac{1}{\lambda_{x_{max}}} \tag{3.7}$$

$$= \frac{\frac{1}{2d_z}}{\left(\frac{1}{2d_z}\right)^2 + \left(\frac{1}{2d_{\lambda_x}}\right)^2} \frac{1}{\lambda_{x_{max}}} \, . \tag{3.8}$$

Theoretically, it is possible to map events in the angle-domain CIG for all reflection angles ranging from zero (corresponding to $k_{\lambda_y} = 0$) to 90° (corresponding to $k_z = 0$). From equation 3.1, for each k_z, the maximum value of $\tan\theta$ mapped from k_{λ_x}, corresponds to the maximum value of this wavenumber, $k_{\lambda_{x_{max}}} = 1/(2d_{\lambda_x})$. As k_z increases, the maximum value of $\tan\theta$ mapped from $k_{\lambda_{x_{max}}}$ decreases and it reaches a minimum for the maximum value of the depth wavenumber $k_{z_{max}}$. For a band-limited lag gather, $k_{z_{max}}$ is the wavenumber that limits the band, i.e., $k_{z_{max}}$ is the maximum k_z frequency that is different from zero. The worst scenario that would have the smallest maximum value of $\tan\theta$ would be for a wide-band lag gather, with $k_{z_{max}}$ corresponding to the Nyquist frequency, in which case $k_{z_{max}} = 1/(2d_z)$. The angle corresponding to $k_{z_{max}}$ is given by

$$\theta_F = \arctan\left(\frac{k_{\lambda_{x_{max}}}}{k_{z_{max}}}\right)$$

$$= \arctan\left(\frac{1}{2d_{\lambda_x}} \frac{1}{k_{z_{max}}}\right) \, , \tag{3.9}$$

where $k_{z_{max}}$ and $k_{\lambda_{x_{max}}}$ are the maximum value for the depth and lag wavenumber, respectively. Thus, not only $k_{z_{max}}$, but also the sample interval in the λ_x dimension, controls θ_F. The angle θ_F defines the range of angles that can be accurately recovered from the lag-domain. For reflection angles greater than θ_F, there is energy defocusing and spreading away from the depth of the reflector in the CIGs. This phenomenon becomes more pronounced for increasing angles. Therefore, even if there is information in the lag gather corresponding to near grazing incidence (90° incidence angle) in the

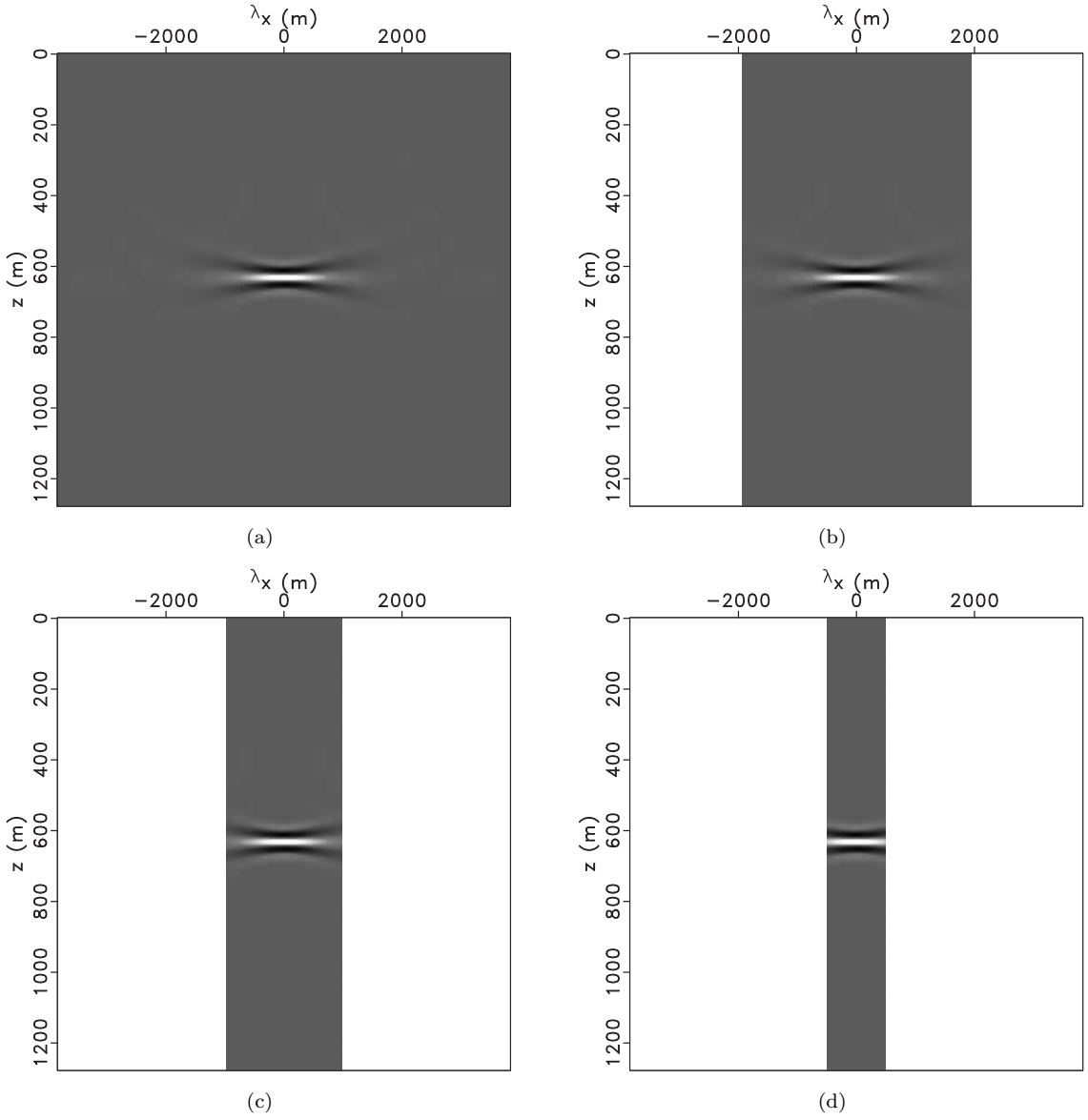

Figure 3.3. Lag gathers with $\lambda_{x_{max}}$ equals to (a) 3840 **m, (b)** 1920 **m, (c)** 960 **m, (d)** 480 **m.**

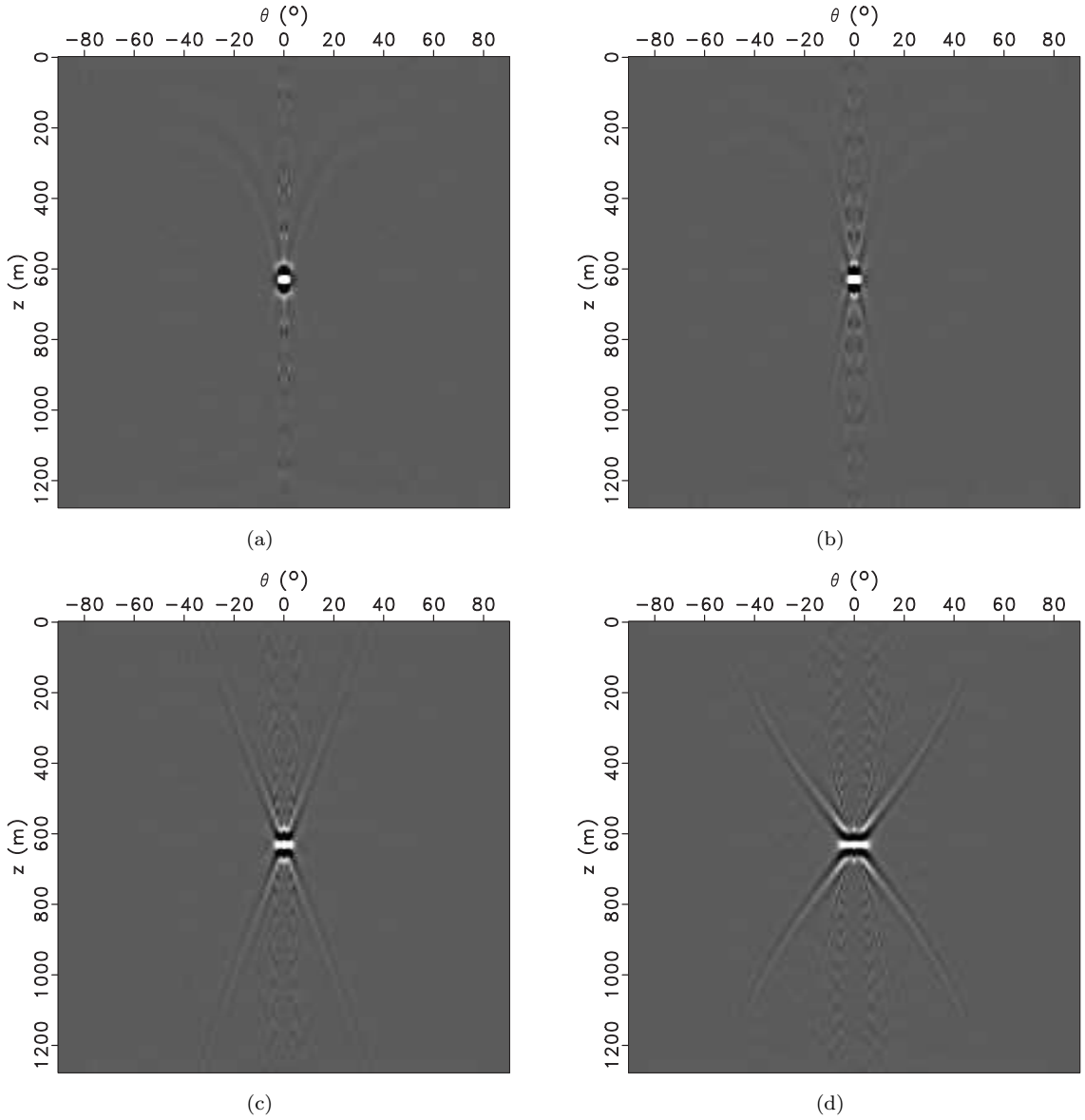

Figure 3.4. Angle gathers corresponding to the lag gathers with $\lambda_{x_{max}}$ equals to (a) 3840 **m, (b)** 1920 **m, (c)** 960 **m, (d)** 480 **m.**

angle gather, when mapped to the angle domain, the energy corresponding to this event is defocused.

In order to analyze and visualize this transformation from lag to angle domain, I consider the idealized case of a lag gather that consists of a spike at depth $z = 640$ m. Ideally, the angle-domain common-image gather obtained from this space-lag-domain gather should contain reflections for the whole range of θ, from zero to $90°$.

The example in Figures 3.5(a) – 3.5(d) illustrates the relationships between angle and space-lag-domain parameters. Figure 3.5(a) represents the synthetic lag gather $I(z, \lambda_x)$ with one single spike located at $z = 640$ and $\lambda_x = 0$ m. Figure 3.5(b) is the 2D Fourier transform $I(k_z, k_{\lambda_x})$ of the lag gather. Figure 3.5(c) shows the result after applying the mapping $k_{\lambda_x} \rightarrow \theta$, according to relation 3.1, to obtain $I(k_z, \theta)$. As discussed earlier, as k_z increases, the mapping from equation 3.1 leads to a decreasing range of $\tan\theta$ for each k_z, which in turn leads to decreasing values of θ. The angle gather $I(z, \theta)$ is shown on Figure 3.5(d). In this example, $d_z = d_{\lambda_x} = 5$ m so, $\theta_F = 45°$. Up to angle θ_F, the energy is well focused at the true depth of the reflector, and after this point it starts to defocus. In $I(k_z, \theta)$, Figure 3.5(c), up to the value $\tan\theta_F = 45$, information exists at all values of k_z and beyond that there is a decrease in information associated with higher absolute values of k_z. One can think of the data in $I(k_z, \theta)$ as the data from $I(k_z, k_{\lambda_x})$ multiplied by a boxcar filter of different width for each k_{λ_x}. Therefore, after applying the inverse Fourier transform on the axis k_z to obtain $I(z, \theta)$, the angles corresponding the the boxcar filtered data appear convolved with a sinc function, and the energy corresponding to these angles defocuses, spreading away from the depth of the reflector, as seen in Figure 3.5(d). Thus, the analysis of angle-domain range involves finding θ_F which is the maximum angle of energy that is well focused at the reflector depth. The relevance of calculating θ_F is that if one wants to use ADCIGs to perform amplitude analysis, the amplitudes for angles greater than θ_F would not be reliable because of the energy spreading effect caused by the angle-mapping transformations.

Figures 3.6(a) – 3.6(d) are similar to Figures 3.5(a) – 3.5(d). All subplots have the same meaning as the ones in the previous example. Since the lag-gather image is band-limited, it does not contain the zero depth wavenumber $k_z = 0$. Therefore, for this more realistic example, there are no reflections corresponding to angles up to $90°$. The highest depth wavenumber is about 0.05 and the maximum lag wavenumber is 0.1, leading to θ_F about $63°$ as seen in Figure 3.8(a).

Figures 3.7(a) – 3.7(d) show lag gathers for different values of d_{λ_x}. In each lag gather, d_{λ_x} is the double of the d_{λ_x} in the precedent gather. Figures 3.8(a) – 3.8(d) are the corresponding angle gathers. We can see that as d_{λ_x} increases, the energy focuses for a smaller range of angles.

In the examples in Figures 3.3(a) – 3.3(d) and Figures 3.4(a) – 3.4(d), we see that the resolution in the angle gathers decreases with the decreasing range in the lag gathers. The bigger the range in the lag domain, the better is the energy focused at the incidence angle in the angle gather.

In the examples in Figures 3.7(a) – 3.7(d) and Figures 3.8(a) – 3.8(d), we see that the range in the angle gathers decreases with the increasing sample interval in the lag gathers.

In the examples in Figures 3.5(a) – 3.5(d) and Figures 3.6(a) – 3.6(d), the reflection energy is not well focused at the reflector depth for angles greater than θ_F. This angle is the ratio between the maximum lag wavenumber and maximum depth wavenumber in the lag gather. In the first example there are no events up to $90°$ in the angle gather because of the energy defocusing that occurs for angles larger than θ_F. For the

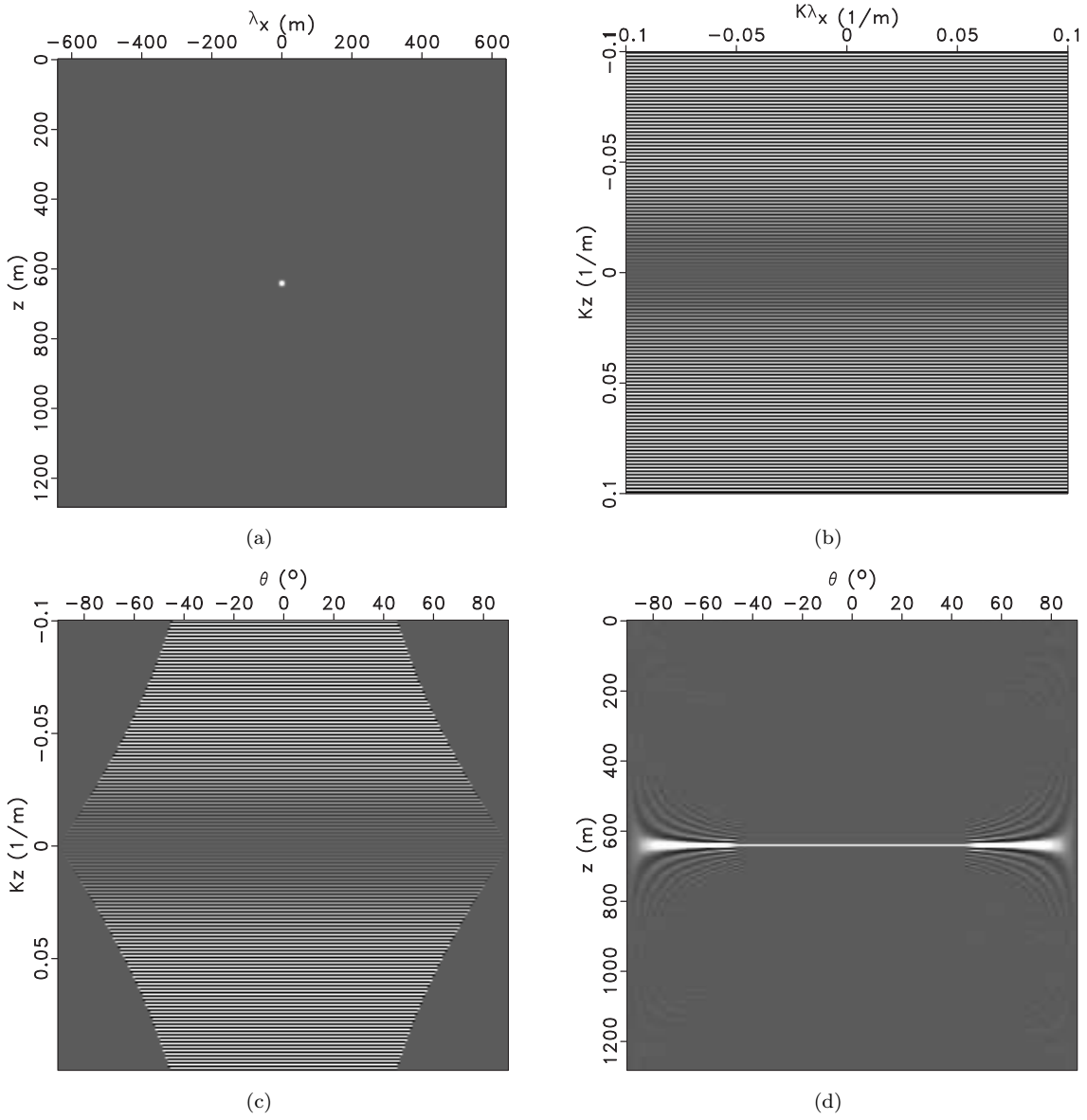

Figure 3.5. Example illustrating mapping from a lag gather with a single spike located at $z = 640$ m and $\lambda_x = 0$ m: (a) lag gather $I(z, \lambda_x)$ with one single spike; (b) 2D Fourier transform $I(k_z, k_{\lambda_x})$ of the lag gather; (c) mapping from k_{λ_x} to θ, $I(k_z, \theta)$; (d) angle-domain common-image gather $I(z, \theta)$.

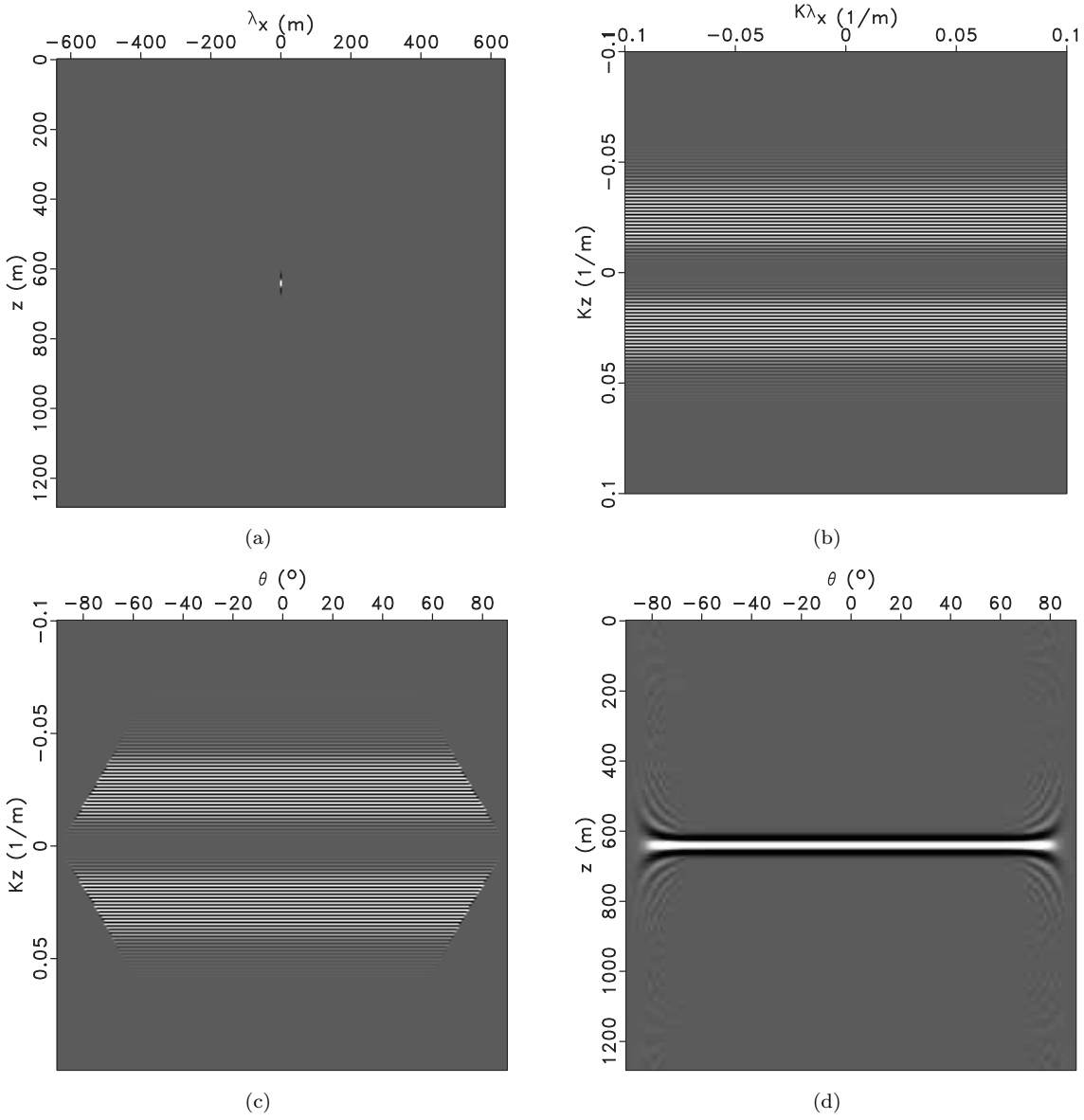

Figure 3.6. Example illustrating mapping from a lag gather with a wavelet located at $z = 640$ m and $\lambda_x = 0$ m: (a) lag gather $I(z, \lambda_x)$ with one single wavelet; (b) 2D Fourier transform $I(k_z, k_{\lambda_x})$ of the lag gather; (c) mapping from k_{λ_x} to θ, $I(k_z, \theta)$; (d) angle-domain common-image gather $I(z, \theta)$.

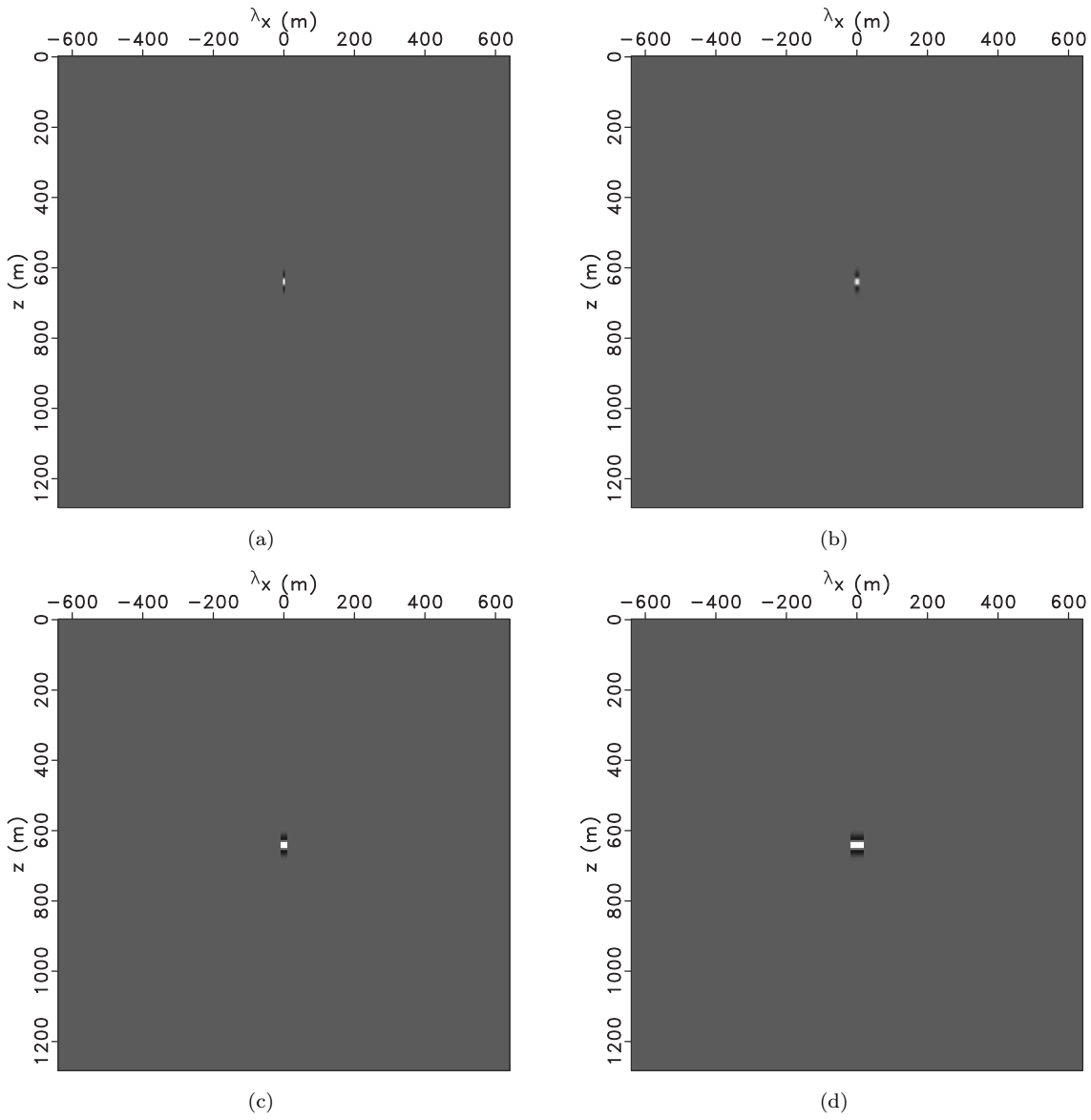

Figure 3.7. Lag gathers with d_{λ_x} equals to (a) 30 m, (b) 60 m, (c) 120 m, (d) 240 m.

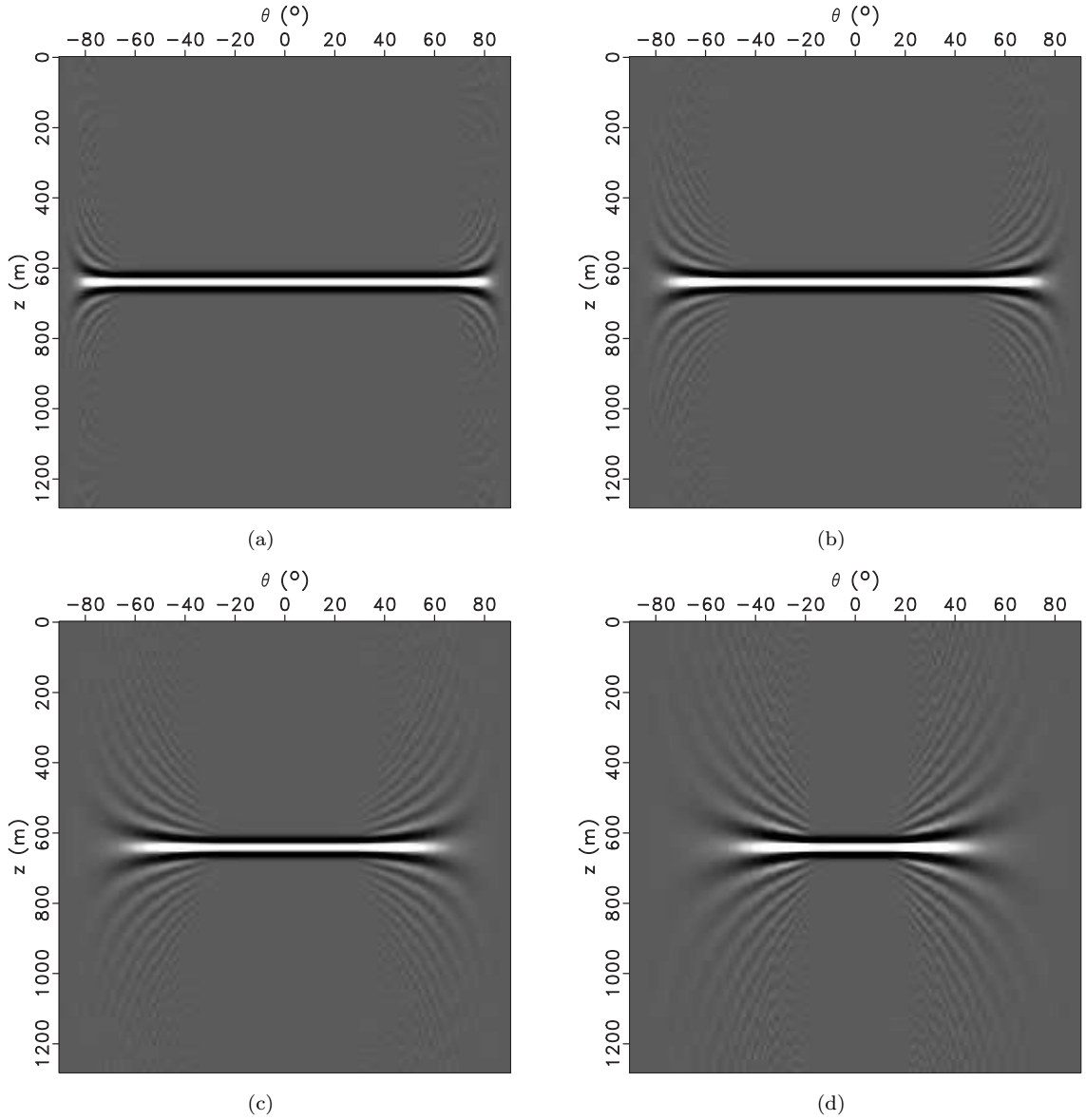

Figure 3.8. Angle gathers corresponding to the lag gathers with d_{λ_x} equals to (a) 30 **m, (b)** 60 **m, (c)** 120 **m, (d)** 240 **m.**

second example, the angle gathers does not have energy at up to 90° because there is no information at $k_z = 0$.

3.2 3D range and resolution analysis

A similar analysis to the one performed in the preceding section can be done for the more general 3D case. Here, the analysis is limited to the case of a horizontal reflector. In this case, the discussion concerns wide-azimuth angle decomposition so, there are two angles for which the range and resolution analysis need to be performed: the reflection angle θ and the azimuthal angle ϕ.

A 3D lag-domain common-image gather can be described as function of two space lags: λ_x and λ_y. The additional 3D model parameters are: origin, sample interval and number of points on the space-lag axis λ_y, $(o_{\lambda_y}, d_{\lambda_y}, n_{\lambda_y})$, on the wavenumber axis k_{λ_y}, $(o_{k_{\lambda_y}}, d_{k_{\lambda_y}}, n_{k_{\lambda_y}})$, and on the azimuthal angle axis ϕ, (o_ϕ, d_ϕ, n_ϕ).

For a 3D horizontal reflector, the reflection angle θ can be computed using the relation

$$\tan\theta = \frac{\sqrt{k_{\lambda_x}^2 + k_{\lambda_y}^2}}{k_z} \; , \tag{3.10}$$

and the azimuthal angle ϕ can be computed using the relation

$$\cos\phi = \frac{k_{\lambda_y}}{\sqrt{k_{\lambda_x}^2 + k_{\lambda_y}^2}} \; . \tag{3.11}$$

Similarly to the 2D case, it is possible to analyze the behavior of d_θ and d_ϕ as functions of k_{λ_x} and k_{λ_y}, i.e., as a function of n_{λ_x} and d_{λ_x}, and n_{λ_y} and d_{λ_y}. Equations 3.10 and 3.11 are rewritten as

$$\theta = \arctan \frac{\sqrt{k_{\lambda_x}^2 + k_{\lambda_y}^2}}{k_z} \; , \tag{3.12}$$

and

$$\phi = \arccos \frac{k_{\lambda_y}}{\sqrt{k_{\lambda_x}^2 + k_{\lambda_y}^2}} \; , \tag{3.13}$$

respectively.

To study how d_θ changes with k_{λ_x} and k_{λ_y}, I differentiate equation 3.12 first with respect to k_{λ_x}

$$d_\theta = \frac{k_z k_{\lambda_x}}{(k_z^2 + k_{\lambda_x}^2 + k_{\lambda_y}^2)\sqrt{k_{\lambda_x}^2 + k_{\lambda_y}^2}} \frac{1}{n_{\lambda_x} d_{\lambda_x}} \; , \tag{3.14}$$

and then with respect to k_{λ_y}

$$d_\theta = \frac{k_z k_{\lambda_y}}{(k_z^2 + k_{\lambda_x}^2 + k_{\lambda_y}^2)\sqrt{k_{\lambda_x}^2 + k_{\lambda_y}^2}} \frac{1}{n_{\lambda_y} d_{\lambda_y}} \; . \tag{3.15}$$

Similarly, to study how d_ϕ changes with k_{λ_x} and k_{λ_y}, I differentiate equation 3.13 first

with respect to k_{λ_x}

$$d_\phi = \frac{1}{\sqrt{1+\dfrac{k_{\lambda_y}^2}{k_{\lambda_x}^2+k_{\lambda_y}^2}}}\frac{-k_{\lambda_x}k_{\lambda_y}}{(k_{\lambda_x}^2+k_{\lambda_y}^2)^{3/2}}\frac{1}{n_{\lambda_x}d_{\lambda_x}} \tag{3.16}$$

and then with respect to k_{λ_y}

$$d_\phi = \frac{1}{\sqrt{1+\dfrac{k_{\lambda_y}^2}{k_{\lambda_x}^2+k_{\lambda_y}^2}}}\frac{k_{\lambda_x}^2}{(k_{\lambda_x}^2+k_{\lambda_y}^2)^{3/2}}\frac{1}{n_{\lambda_y}d_{\lambda_y}} \tag{3.17}$$

Equations 3.14, 3.15, 3.16, and 3.17 show that d_θ and d_ϕ are both inversely proportional to $n_{\lambda_x}d_{\lambda_x} = \lambda_{x_{max}}$ and $n_{\lambda_y}d_{\lambda_y} = \lambda_{y_{max}}$, where the parameters $\lambda_{x_{max}}$ and $\lambda_{y_{max}}$ are the ranges in space-lag domain, which control the resolution in the angle domain. As in the preceding section, I conclude that the larger the range in the space-lag domain, the better the resolution in the angle domain.

To observe the influence of $\lambda_{x_{max}}$ and $\lambda_{y_{max}}$ on d_θ and d_ϕ described on equations 3.14 – 3.17, I construct an example where I create angle gathers from lag gathers with different ranges $\lambda_{x_{max}}$ and $\lambda_{y_{max}}$.

Figure 3.9 is a migrated image that shows a horizontal reflector located at $z = 640$ m. The source is located on the center of the horizontal grid, $x = y = 3840$ m.

Figure 3.10(a) is the lag-domain CIG constructed at the same horizontal locations as the source. Thus, at this location, the reflection corresponds to normal incidence. The lag ranges $\lambda_{x_{max}}$ and $\lambda_{y_{max}}$ in this case cover the whole x and y dimensions, respectively. Both x and y axis go from 0 to 7680 m. Since the lag axes are centered at 0, they go from -3840 to 3840 m, i.e., $\lambda_{x_{max}} = \lambda_{y_{max}} = 3840$ m. Figure 3.10(b) is the Fourier transform of the lag gather and Figure 3.10(c) shows the image obtained after applying transformations 3.12 and 3.13 to the image in Figure 3.10(b). Figure 3.10(d) is the corresponding angle gather, which shows a reflection at $\theta = 0°$, as expected.

Next, I create four new lag gathers and each one has $\lambda_{x_{max}}$ and $\lambda_{y_{max}}$ half of their values in the previous gather, Figures 3.11(a) – 3.11(d). Figures 3.12(a) – 3.12(d) are the angle gathers corresponding to the lag gathers in Figures 3.11(a) – 3.11(d). Observe in Figures 3.12(a) – 3.12(d) that the smaller the range in the lag domain, the worse the resolution in the angle domain, as expected from equations 3.14 – 3.17.

Using similar arguments to the ones employed for the 2D analysis, to uniformly sample the angle-domain and avoid aliasing, the parameters d_θ and d_ϕ need to be lesser or equal to their minimum possible values given by substituting the wavenumbers in equations 3.14, 3.15, 3.16,and 3.17 by their maximum values (Nyquist). This way, there are two possible values for both d_θ and d_ϕ, and the minimum of the two should be used in each case.

Equation 3.12 shows that, for each k_{λ_y} there is an angle that can be mapped from the lag domain, given by $k_{\lambda_{x_{max}}}$ and $k_{z_{max}}$ (as defined in previous section), that limits the range of angles for which there is information at all values of k_z. I define θ_F in 3D as the smallest of these angles, which corresponds to $k_{\lambda_y} = 0$ in equation 3.12. This angle θ_F defines the range of reflection angles that can be accurately recovered from the lag domain, because this range of angles contains information for all depth wavenumbers k_z for all azimuths. The maximum θ for which there is information at all wavenumbers k_z changes with ϕ. Outside the range defined by θ_F, due to the fact that this maximum

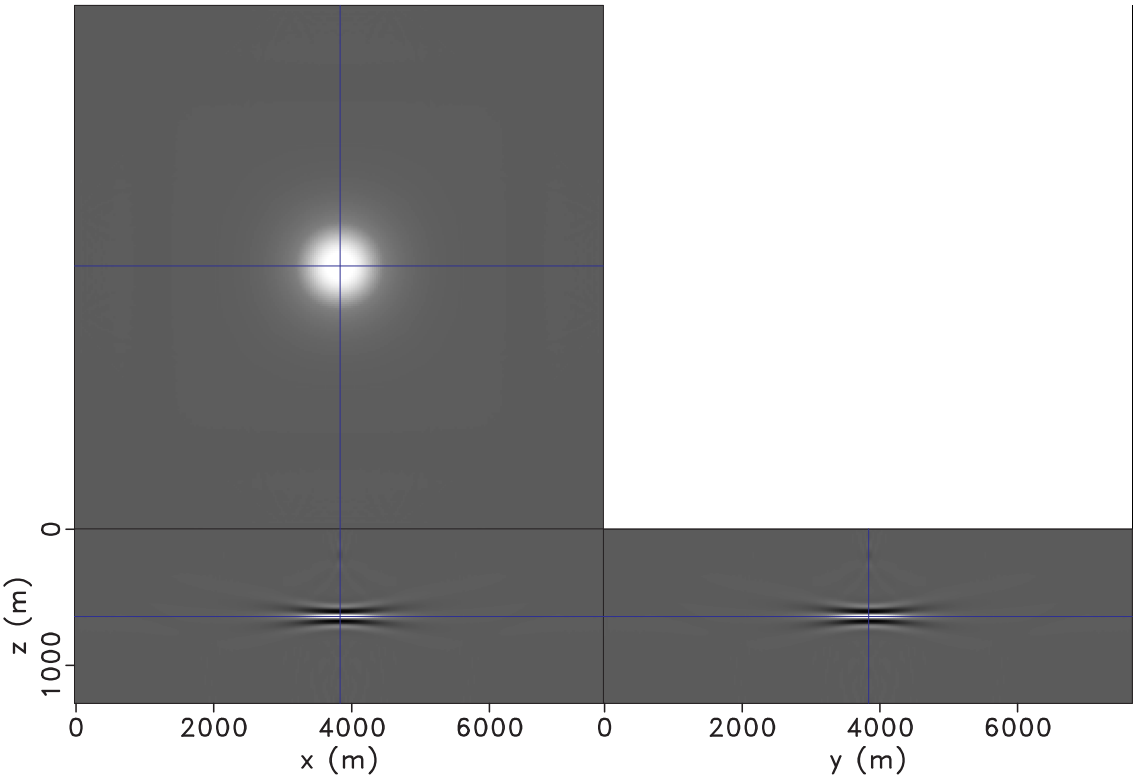

(a)

Figure 3.9. Migrated image $I(x, y, z)$: 3D flat reflector located at $z = 640$ m. The source is located at $z = 0$ and $x = y = 3840$ m.

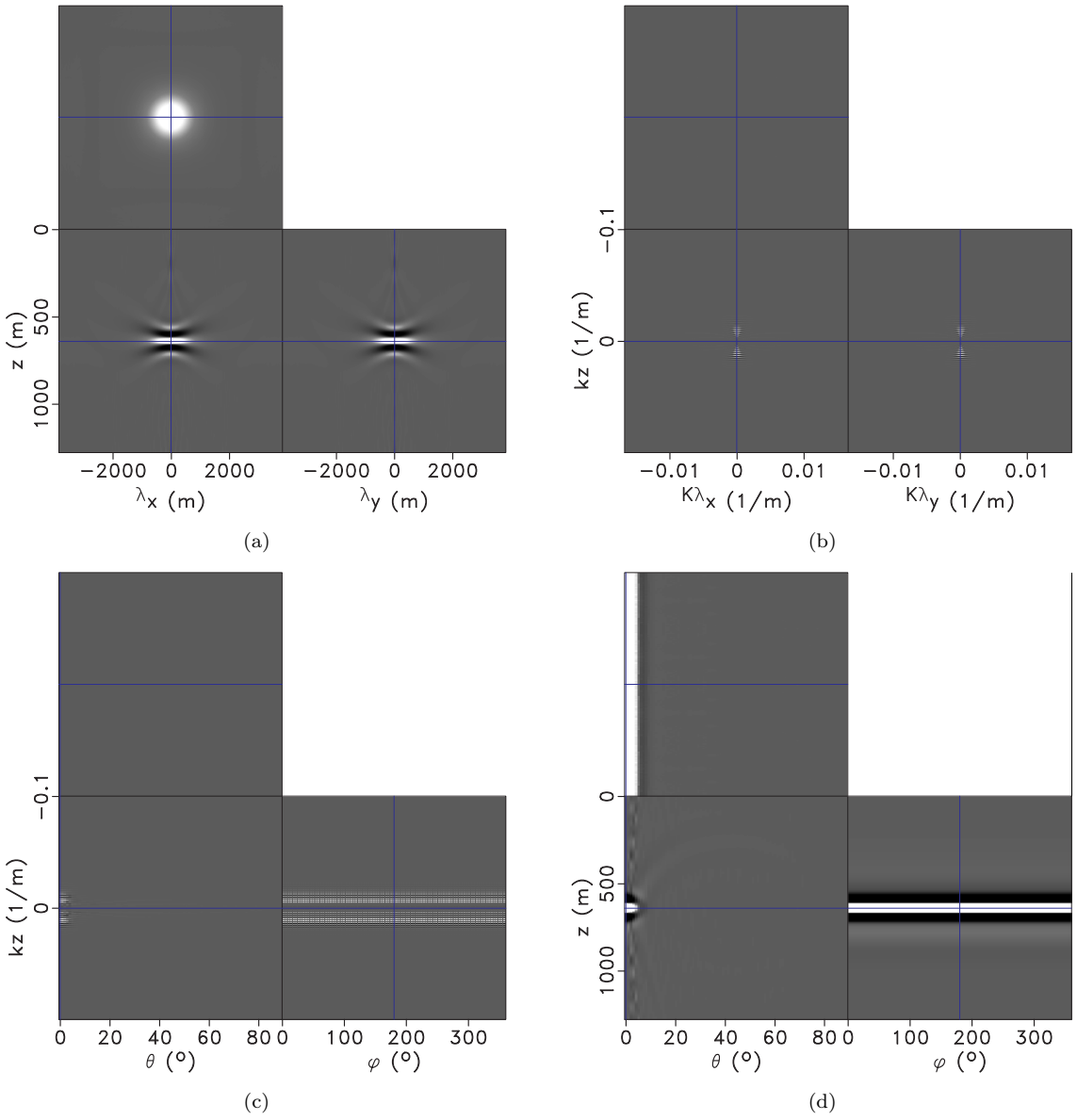

Figure 3.10. Construction of angle gather from lag gather for example of 3D flat reflector located at $z = 640$ m: (a) lag gather $I(z, \lambda_x, \lambda_y)$; (b) lag gather in the Fourier domain $I(k_z, k_{\lambda_x}, k_{\lambda_y})$; (c) mapping from $(k_{\lambda_x}, k_{\lambda_y})$ to (θ, ϕ), $I(k_z, \theta, \phi)$; (d) angle-domain common-image gather $I(z, \theta, \phi)$.

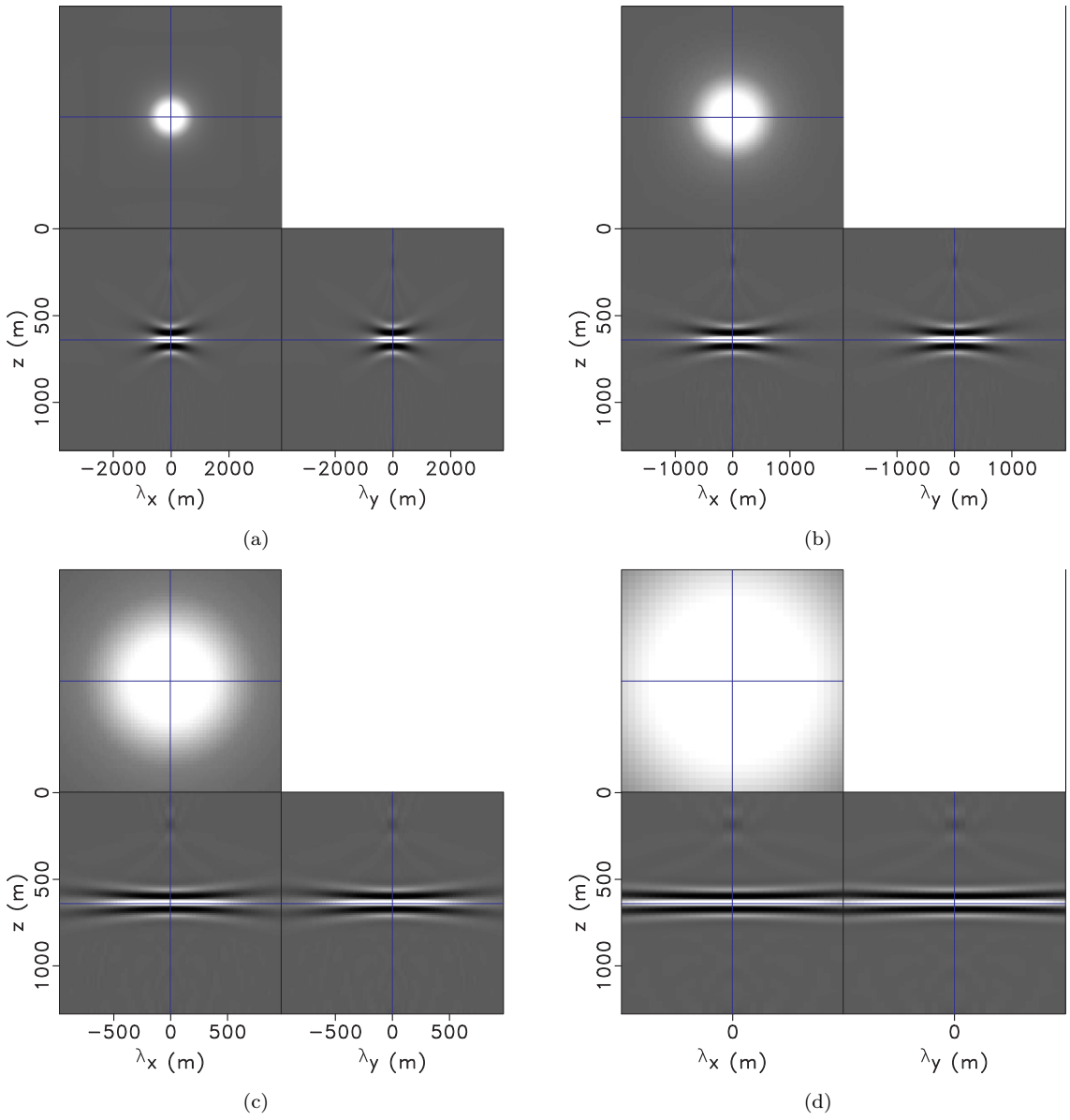

Figure 3.11. Lag gathers with $\lambda_{x_{max}} = \lambda_{y_{max}}$ equals to (a) 3840 **m, (b)** 1920 **m, (c)** 960 **m, (d)** 480 **m.**

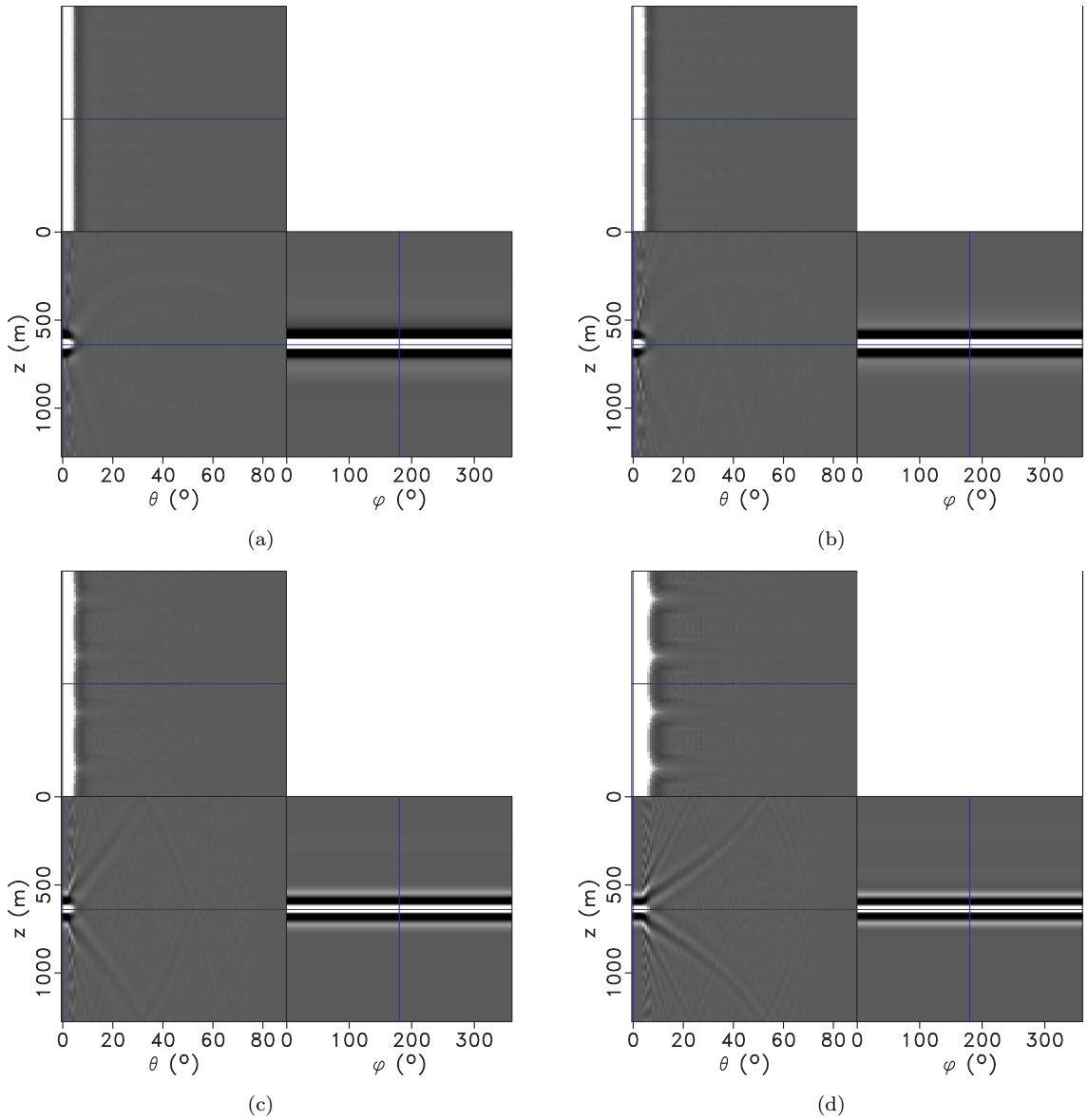

Figure 3.12. Angle gathers corresponding to the lag gathers with $\lambda_{x_{max}} = \lambda_{y_{max}}$ equals to (a) 3840 **m, (b)** 1920 **m, (c)** 960 **m, (d)** 480 **m.**

θ changes with ϕ, there is an uneven information distribution along the ϕ dimension, with respect to k_z. The azimuthal angles 45, 135, 225, and 315° have more information at more wavenumbers k_z than the other angles (due to a squared grid used in this example), and there is a decrease on this wavenumbers as angles depart from these four values, reaching a minimum at 0, 90, 180, and 270°. Thus, reflections occurring at these four azimuthal angles where there is more information, or in their vicinity, have better focused events in the angle gathers than at other azimuthal angles.

Similarly to the 2D case, I construct synthetic 3D lag-gathers (first with a spike and then with a band-limited wavelet at zero lag in x and y) and study the steps involved in the implementation of the mappings described in equations 3.10 and 3.11.

For the first example, I construct a lag gather $I(z, \lambda_x, \lambda_y)$ with a spike at $(z = 640, \lambda_x = 0, \lambda_y = 0)$. Then, I apply a 3D Fourier transform on the lag gather to obtain $I(k_z, k_{\lambda_x}, k_{\lambda_y})$. Next, I apply the mapping equations 3.10 and 3.11 to get $I(k_z, \theta, \phi)$. Finally, I apply the inverse Fourier transform to the k_z dimension to create the angle gather $I(z, \theta, \phi)$. Figures 3.13(a) to 3.13(d) shows four 3D plots representing the image in these four domains. In each of the 3D plots, the cross lines show the position of the sections displayed on the flat images. Figure 3.13(a) is the lag gather, $I(z, \lambda_x, \lambda_y)$, with one single spike. Figure 3.13(b) is the 3D Fourier transform, $I(k_z, k_{\lambda_x}, k_{\lambda_y})$, of the lag gather. Figure 3.13(c) shows both mappings from equations 3.10 and 3.11 applied to $I(k_z, k_{\lambda_x}, k_{\lambda_y})$ to obtain $I(k_z, \theta, \phi)$. For this wide-band example $\theta_F = 45$ because the lag gather has information for all wavenumbers (wide-band) and the sample interval in all dimensions are equal. In the (k_z, θ) cross-section in Figure 3.13(c), for angles θ up to 45° information exists at all wavenumbers k_z, and for angles greater than 45° there is an uneven information distribution along the ϕ dimension, with respect to k_z. The azimuthal angles 45, 135, 225, and 315° have more information at more wavenumbers k_z than the other angles, and there is a decrease on this wavenumbers as angles depart from these four values, reaching a minimum at 0, 90, 180, and 360°. The same pattern can be been in the (k_z, ϕ) cross-section in this same figure. For the reflection angles in the interval $|\theta| <= 45$, the energy is well focused in the angle gathers for all azimuthal angles.

As in the 2D case, for the next example, I construct a 3D lag gather with a wavelet rather than a spike, with the intent of simulating a more realistic situation (a band-limited lag gather). Figures 3.14(a) – 3.14(d) shows, respectively, $I(z, \lambda_x, \lambda_y)$, $I(k_z, k_{\lambda_x}, k_{\lambda_y})$, $I(k_z, \theta, \phi)$, $I(z, \theta, \phi)$. The wavelet in the 3D lag gather is band limited and the maximum depth wavenumber is smaller than the Nyquist frequency $k_{z_{max}}$. That causes the angle θ_F for this case to be greater than for the previous example. Therefore, in this case, the range of angles for which the energy is well focused in the 3D angle-domain common-image gather, for all azimuthal angles, is larger than for the spike-lag example (around 63°). As for the preceding example, the angle θ_F changes with azimuth reaching maximum values at $\phi =$ 45, 135, 225, and 315°.

Figures 3.15(a) – 3.15(d) show lag gathers for different values of d_{λ_x}. In each lag gather, d_{λ_x} is the double of the d_{λ_x} in the precedent gather. Figures 3.16(a) – 3.16(d) are the corresponding angle gathers. We can see that as d_{λ_x} increases, the energy focuses for a smaller range of angles.

According to the analysis performed in this chapter, I conclude that when implementing the extended imaging condition one should use the smallest sample interval that is available for the space lags, which is the same sample interval as for the corresponding space coordinates. In the numerical examples that I present in the next chapter, I use about 20 percent of the number of samples in the space domain to

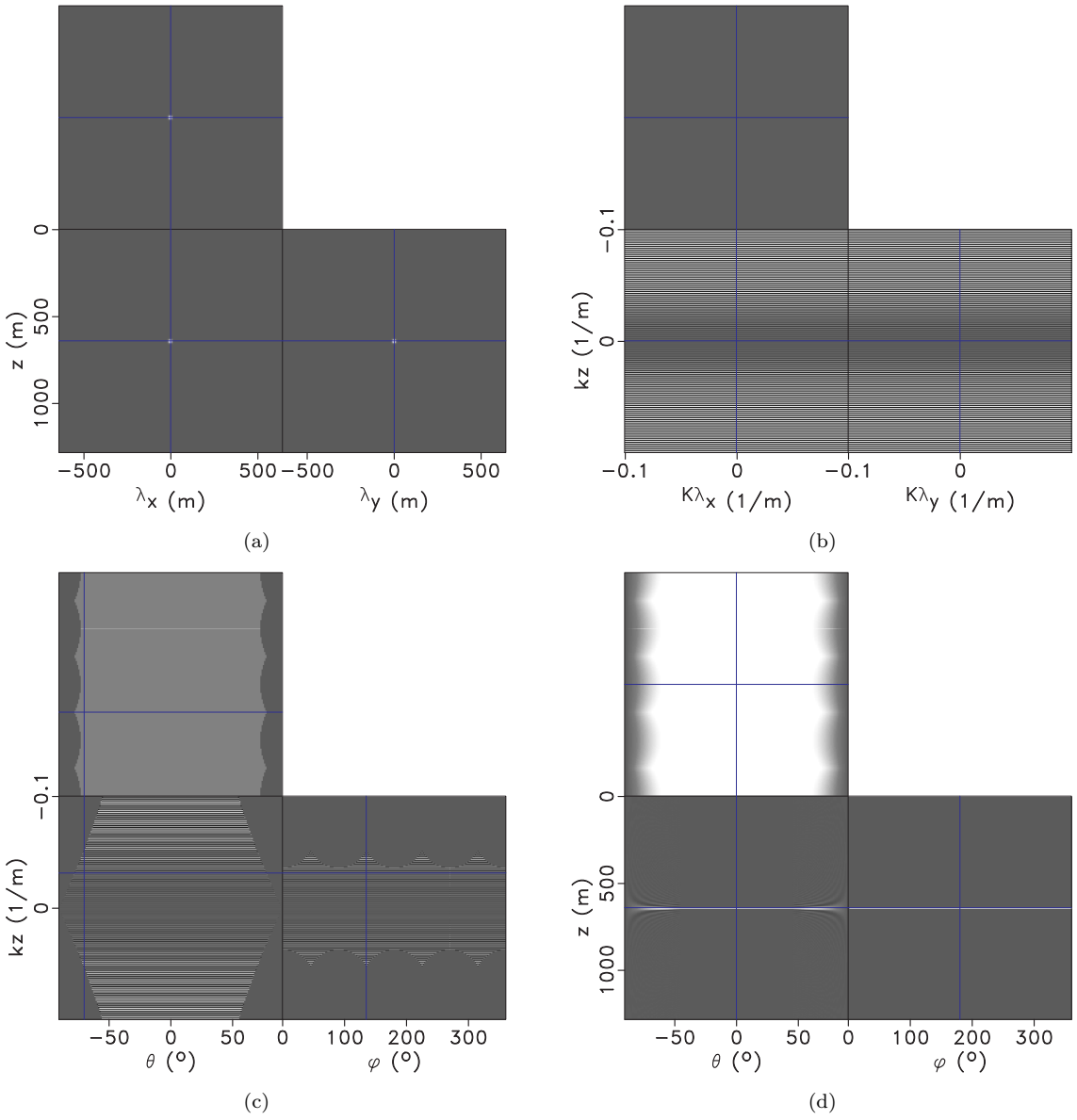

Figure 3.13. Example illustrating mapping from a 3D lag gather with a single spike located at $z = 640$ m and $\lambda_x = \lambda_y = 0$ m: (a) lag gather $I(z, \lambda_x, \lambda_y)$ with one single spike; (b) 3D Fourier transform of the lag gather $I(k_z, k_{\lambda_x}, k_{\lambda_y})$; (c) mapping from $(k_{\lambda_x}, k_{\lambda_y})$ to (θ, ϕ), $I(k_z, \theta, \phi)$; (d) angle-domain common-image gather $I(z, \theta, \phi)$.

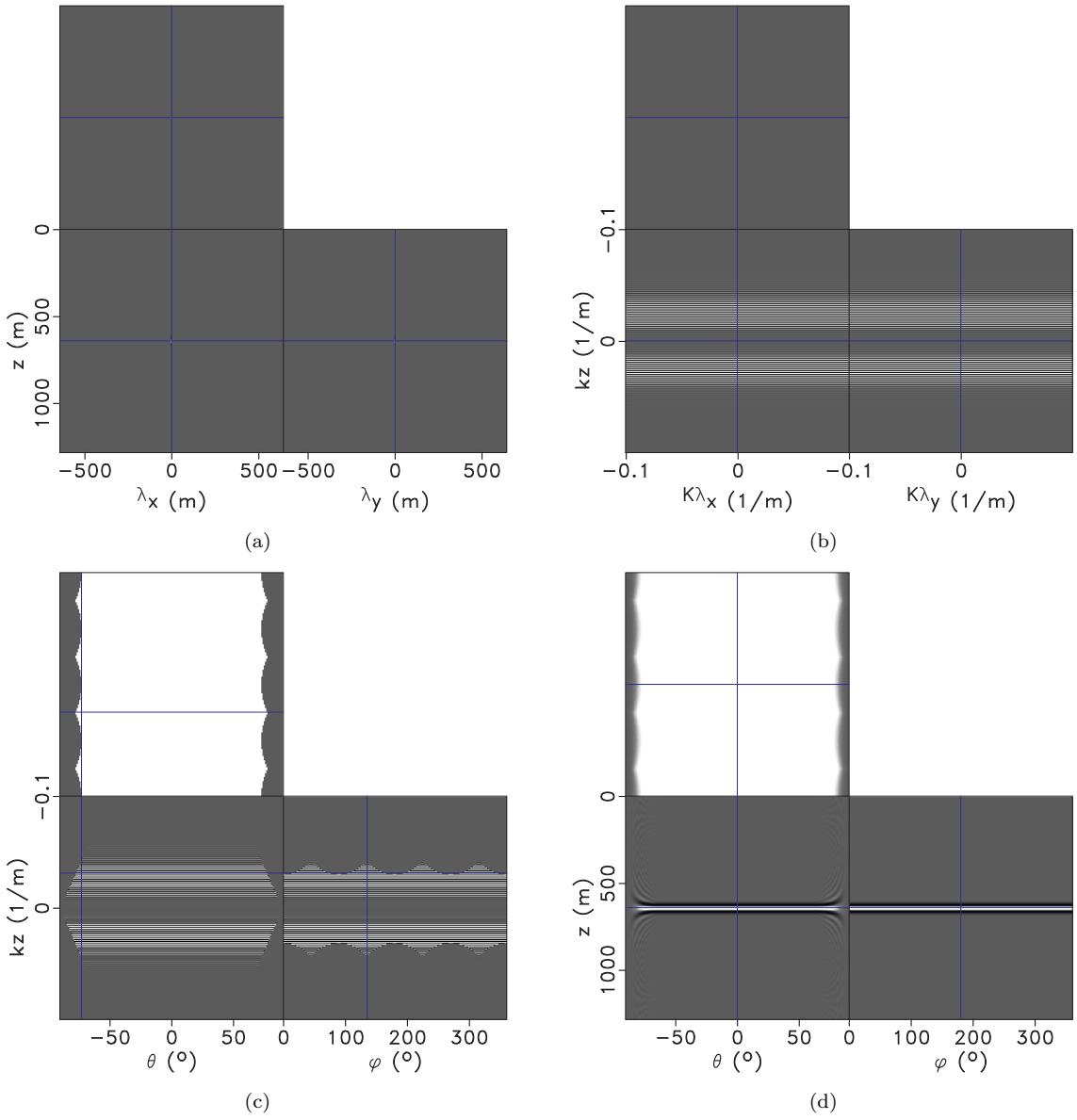

Figure 3.14. Example illustrating mapping from a 3D lag gather with a wavelet located at $z = 640$ m and $\lambda_x = \lambda_y = 0$ m: (a) lag gather $I(z, \lambda_x, \lambda_y)$ with one single wavelet; (b) 3D Fourier transform of the lag gather $I(k_z, k_{\lambda_x}, k_{\lambda_y})$; (c) mapping from $(k_{\lambda_x}, k_{\lambda_y})$ to (θ, ϕ), $I(k_z, \theta, \phi)$; (d) angle-domain common-image gather $I(z, \theta, \phi)$.

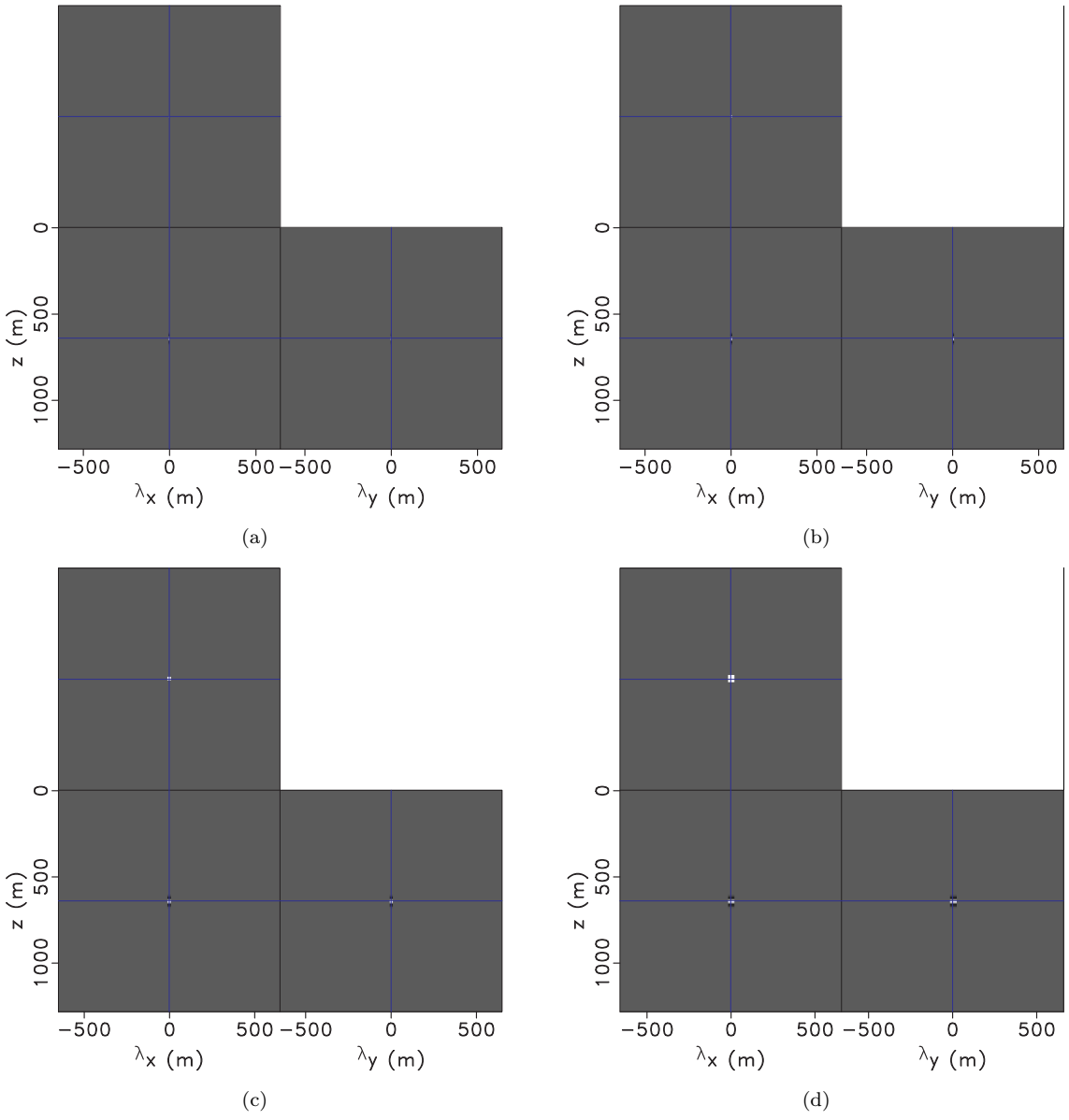

Figure 3.15. Lag gathers with $d_{\lambda_x} = d_{\lambda_y}$ equals to (a) 30 m, (b) 60 m, (c) 120 m, (d) 240 m.

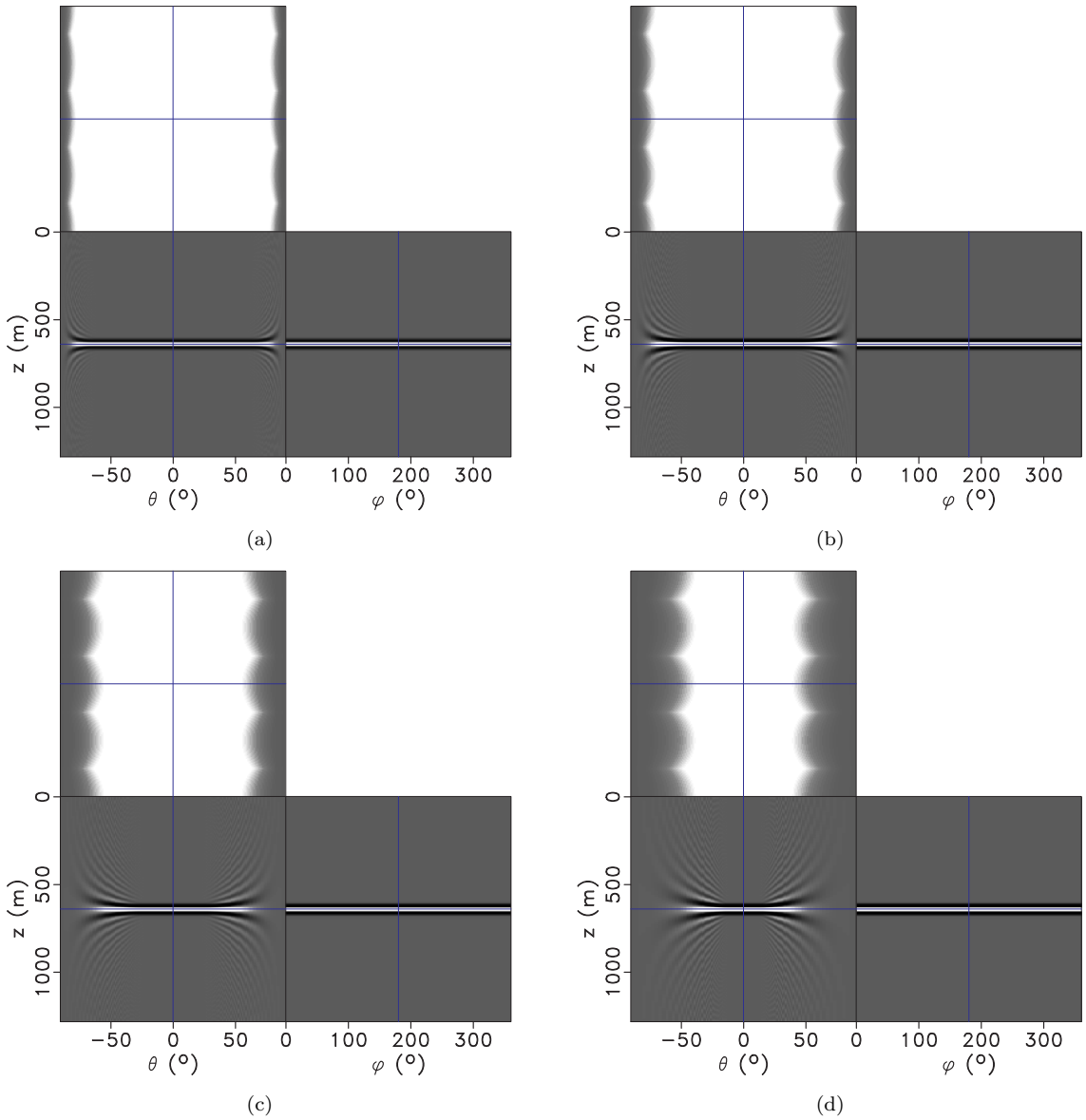

Figure 3.16. Angle gathers corresponding to the lag gathers with $d_{\lambda_x} = d_{\lambda_y}$ equals to (a) 30 m, (b) 60 m, (c) 120 m, (d) 240 m.

construct the lag domain.

Given the sampling parameters used to construct the extended image one can estimate the range of usable angles in the angle gathers using the relationships discussed in this chapter. When constructing the angle gathers, the parameters to be chosen are the sample intervals for both angles. They should be chosen observing the aliasing issue previously discussed to make sure that the angle gathers are not aliased.

Chapter 4

Synthetic examples

I present two examples of angle decomposition analysis in this chapter. The first example is a simple homogeneous model with a horizontal reflector and is meant to show the difference, in the angle gathers, for reflections inside and outside the range discussed in Chapter 3. I create two scenarios with different velocity models and construct nine CIGs for the same locations in both cases. In the first case, the reflections occur at reflection angles that are inside the range mentioned above and, in the second case, the reflections occur at larger angles. Observing the angle gathers for these two situations we can see how different the energy focus is for these two cases. The second example demonstrates the analysis of Chapter 3 in a more complex situation where I use the SEG/EAGE salt dome model to create the data and the images. In this example, I show only one CIG containing many reflections, where some of them are inside and some are outside the range of usable angles.

4.1 Depth dependent velocity $v(z)$ and/or dipping reflectors

The following first two examples are meant to illustrate the relationships discussed in preceding chapters. I create these examples with the same geometry but different velocity models. In both examples the velocity varies with depth, $v = v(z)$, but with negative and positive gradients, respectively. I construct CIGs for the same locations in both cases, as illustrated in Figure 4.1. For the first example, the reflection angles for these CIG locations are within the range of well focused energy discussed in the previous section, i.e., the reflection angles at these locations are smaller than θ_F for each gather. In this case, the energy in the angle gathers are well focused. In the second example, the reflection angles in all gathers but one are greater than θ_F, and in this case the energy is less well focused.

The reflectivity model is a horizontal reflector embedded in a $v = v(z)$ medium. The model parameters are: $(o_x, d_x, n_x) = (0, 30, 180)$, $(o_y, d_y, n_y) = (0, 30, 180)$, and $(o_z, d_z, n_z) = (0, 5, 180)$. There is one source located in the center of the horizontal plane. The reflector is located at depth $z_r = 700$ m. The velocity model for the first example is $v(z) = 4500 - 4z$. The synthetic data (due to one source) $D(\boldsymbol{x}, t)$ and migrated image $I(\boldsymbol{x})$ are shown are Figure 4.2. There, we can see the flat reflector located at depth $z_r = 700$m.

As discussed earlier, I construct ADCIGs just for some locations over the reflector. In the hypercube image $I(\boldsymbol{x}, \boldsymbol{\lambda})$, one can select a location in the horizontal space, $(x, y) = (x_0, y_0)$, where one wants to construct an ADCIG, and obtain the three-dimensional subset $I_h = I(x = x_0, y = y_0, z, \lambda_x, \lambda_y, \lambda_z = 0)$. Figure 4.3 shows lag gathers for nine different locations at the reflector (Figure 4.1). Each gather is obtained by selecting the depth of the reflector, thus, each gather represents the set $I_h = I(x = x_0, y = y_0, z =$

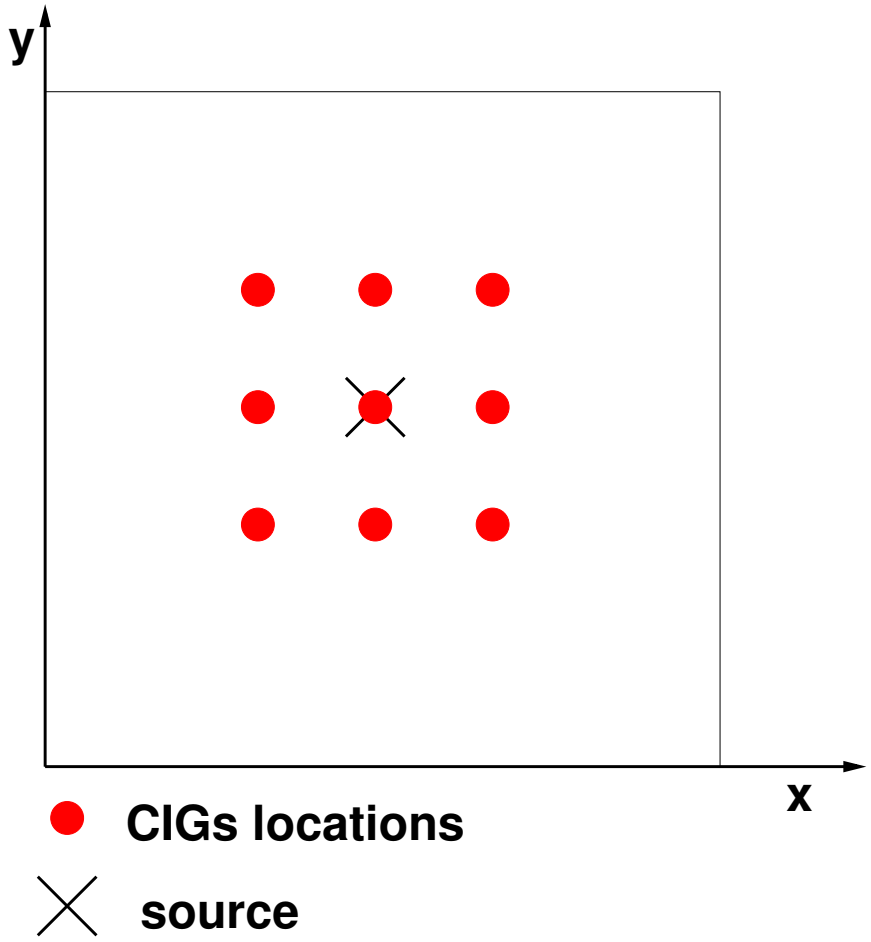

Figure 4.1. CIG locations. Each circle is a CIG location and the cross is the source location. The central CIG horizontal location is the same as the source location. The CIGs around the central one are 300 meters apart in one or both x and y directions.

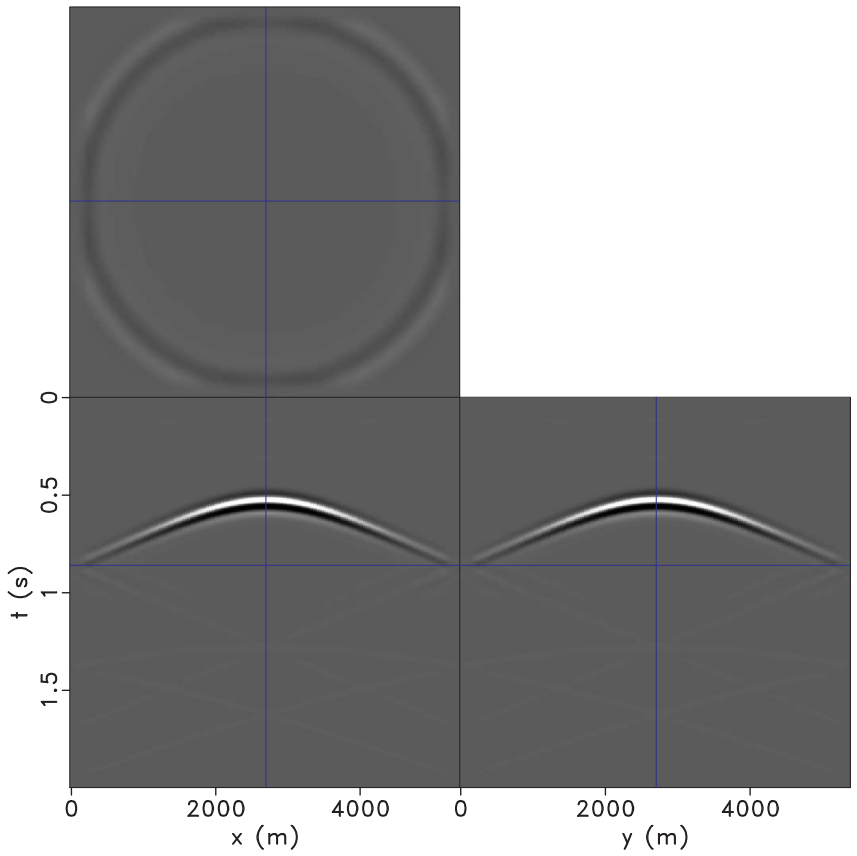

(a)

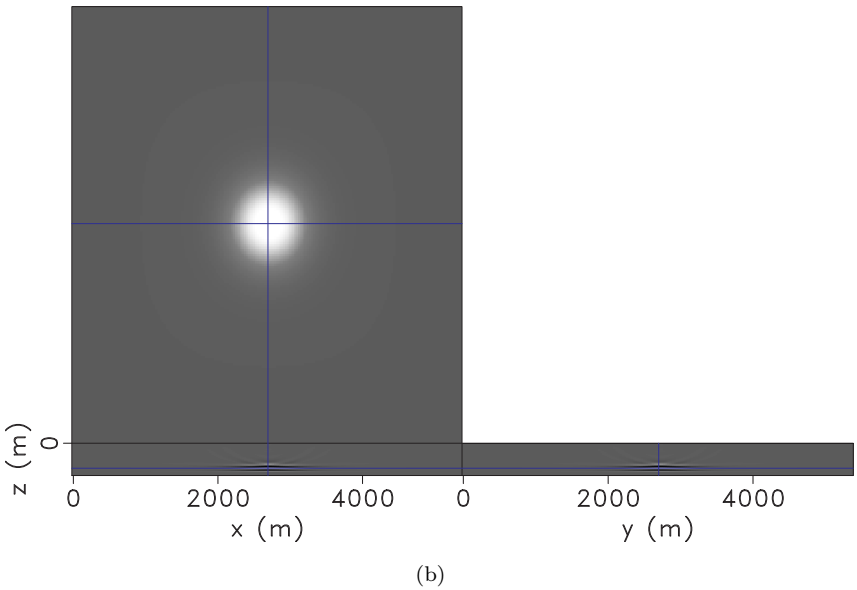

(b)

Figure 4.2. (a) Data for the one shot located at center of x-axis, and (b) image of horizontal reflector located at $z_r = 700$ m.

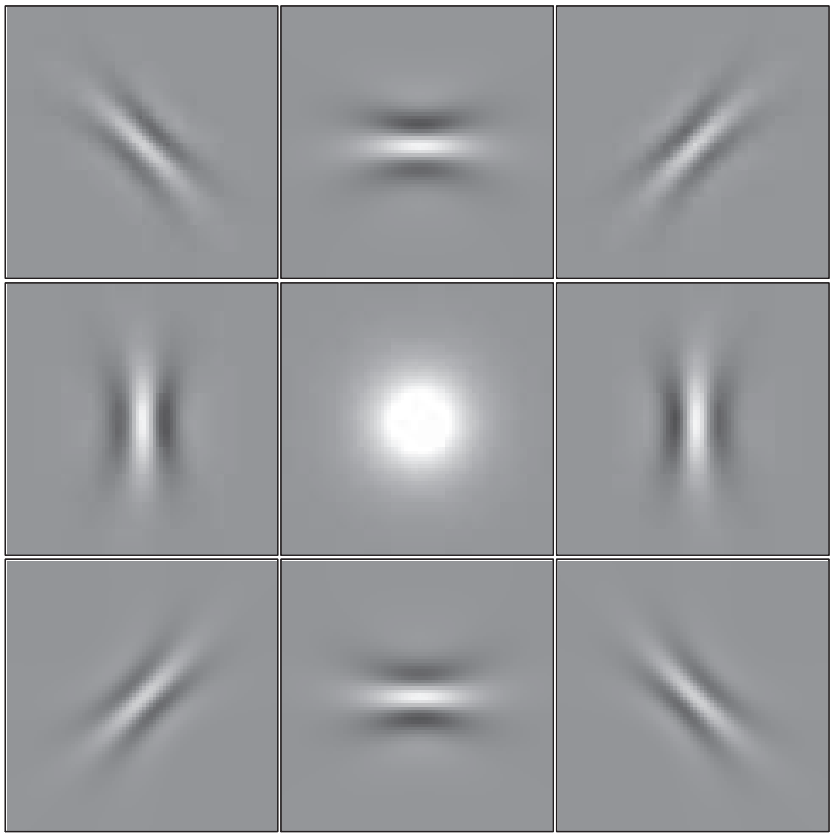

Figure 4.3. Space-lag domain common-image gathers: each individual plot is a lag gather for a different horizontal location over the reflector. In each figure, the horizontal axis is λ_x and the vertical is λ_y. The gather in the center has the same horizontal location as the source. The gathers around the central one are located 300 m away from it in one or both horizontal directions.

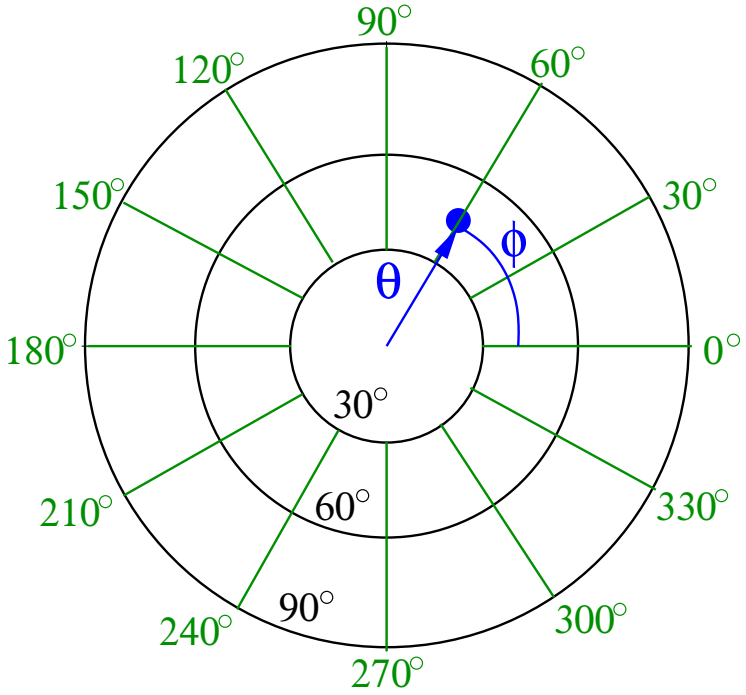

Figure 4.4. Polar representation of reflection energy as a function of reflection and azimuthal angle: The azimuthal angle ϕ is zero in the positive horizontal direction and increases in the counter-clockwise direction. The distance from the center of the circles to the event represents the angle θ, which has a minimum value of zero for events appearing in the center of the figure, and a maximum value of 90 for events located on the outer circle. The filled dot represents a reflection event where $\theta = 45°$ and $\phi = 60°$.

$z_r, \lambda_x, \lambda_y, \lambda_z = 0$). The gather in the center has the same horizontal location as the source. The gathers around it are located 300 m from the central location in one or both coordinate directions. For each panel in Figure 4.3, the horizontal axis is λ_x and the vertical is λ_y.

I create an angle gather for each lag gather. To better visualize an ADCIG, I make use of polar plots. Figure 4.4 helps in locating and understanding how an event appears on a polar plot. The azimuthal angle ϕ is zero in the positive horizontal direction and increases in the counter-clockwise direction. The distance from the center of the circles to the event represents the angle θ, which has a minimum value of zero for events appearing in the center of the figure, and a maximum value of $90°$ for events located on the outer circle. The angle gathers obtained from the lag gathers in Figure 4.3 are shown in Figure 4.5.

Since the medium is homogeneous and the reflector is horizontal, the azimuth of the reflection plane coincides with the source-receiver azimuth on the surface, as can be seen in Figure 4.5. The central polar plot corresponds to the image point right under the source and, as expected, there is an event at $\theta = 0°$, i.e., there is normal incidence at this point. We can see in these gathers that the energy is well focused, as expected,

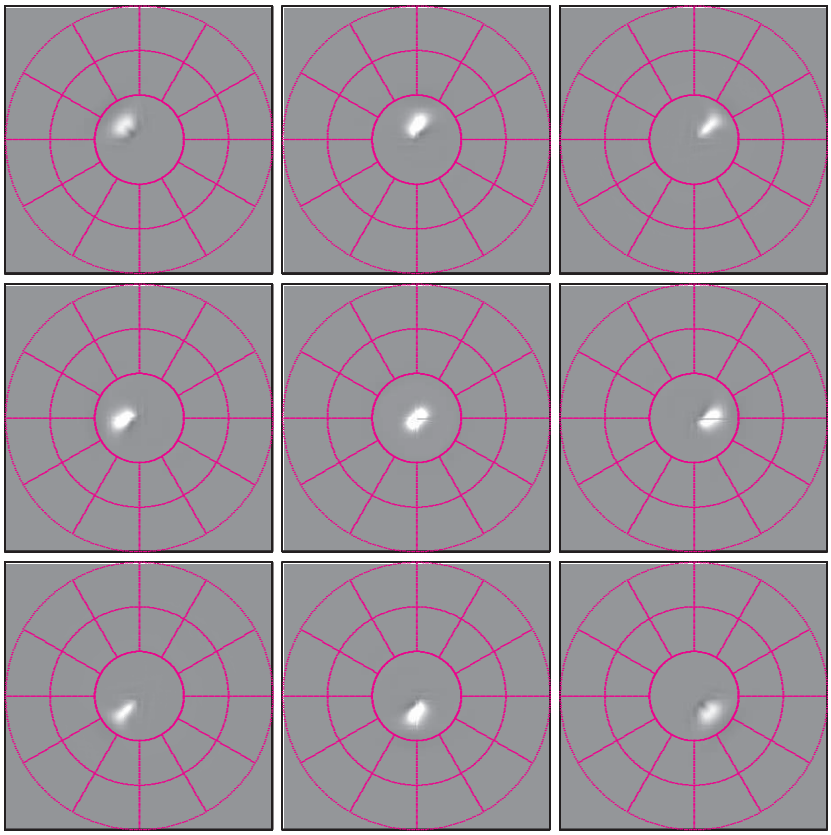

Figure 4.5. Angle-domain common-image gathers: each individual plot is the angle gather (CIG) obtained from the lag gathers in Figure 4.3. The gathers are displayed in a polar plot format. Refer to Figure 4.4 for a polar plot interpretation.

since the reflection angles are within the range of accurately recovered reflections.

The velocity model for the second example is $v(z) = 1000 + 4z$. The synthetic data $D(x, y, t)$ and migrated image $I(\boldsymbol{x})$ are shown in Figure 4.6. There, we can see the flat reflector located at depth $z_r = 700$m.

Figure 4.7 shows nine lag gathers for the same nine locations in the previous example. Each gather is also obtained by selecting the depth of the reflector in $I_h = I(x = x_0, y = y_0, z = z_r, \lambda_x, \lambda_y, \lambda_z = 0)$. The angle gathers obtained from the lag gathers in Figure 4.7 are shown in Figure 4.8.

As can be seen in Figure 4.8 the energy is less well focused compared to Figure 4.5. That is because the reflection angles are outside the range of well focused energy defined by the angle θ_F explained in the preceding sections. The central CIG looks defocused even though the reflection angle is zero at this location. This is due to a low clip value used to create the plots in that case. We can see through these two examples how energy focuses well or not depending on whether the reflection angles are inside or outside the range of well-focused angles. The angles θ and ϕ in the images are validated by expressions found in Dobrin (1988).

4.2 SEG/EAGE salt dome model

In order to perform the range and resolution analysis discussed in this work, I use a more realistic example, although still synthetic. I use the SEG/EAGE salt dome model as velocity and reflectivity model to create synthetic data. Figure 4.9 shows the the location of 31 sources in relation to the CIG location. Figure 4.10 shows the velocity and reflectivity model. Figure 4.11 shows the migrated image. The horizontal lines in Figure 4.10 and Figure 4.11 show the location of the CIG. I used 30 shots distributed around the CIG location. The range size of the horizontal axis x and y for each shot is $x = y = 4000$ m. In this example I constructed the CIGs with 30 grid points on the lag axis, so $\lambda_{x_{max}} = \lambda_{y_{max}} = 300$ m.

Figure 4.12(a) shows the angle-domain CIG for one shot. The reflection angle in this case is approximately $\theta = 30^\circ$. Figure 4.12(b) shows the angle-domain CIG for another shot location. The reflection angle in this case is approximately $\theta = 55^\circ$. In both figures we clearly see the reflections. Figure 4.12(c) shows the angle-domain CIG for all the shots together. We clearly see the reflection corresponding to 30° but we barely see the reflection corresponding to 55°. Performing the range and resolution analysis studied in this work, I conclude that for this example, the bound of the range of usable angles would be $\theta_F = 35^\circ$. Thus, when I plot the CIGs all together as in Figure 4.12(c) the amplitude of the reflection with $\theta = 30^\circ$, which is inside the range, is higher than the one with greater $\theta = 55^\circ$, which is outside the range.

In all the examples in this work, I use the angle decomposition method based on the work of Sava & Fomel (2005).

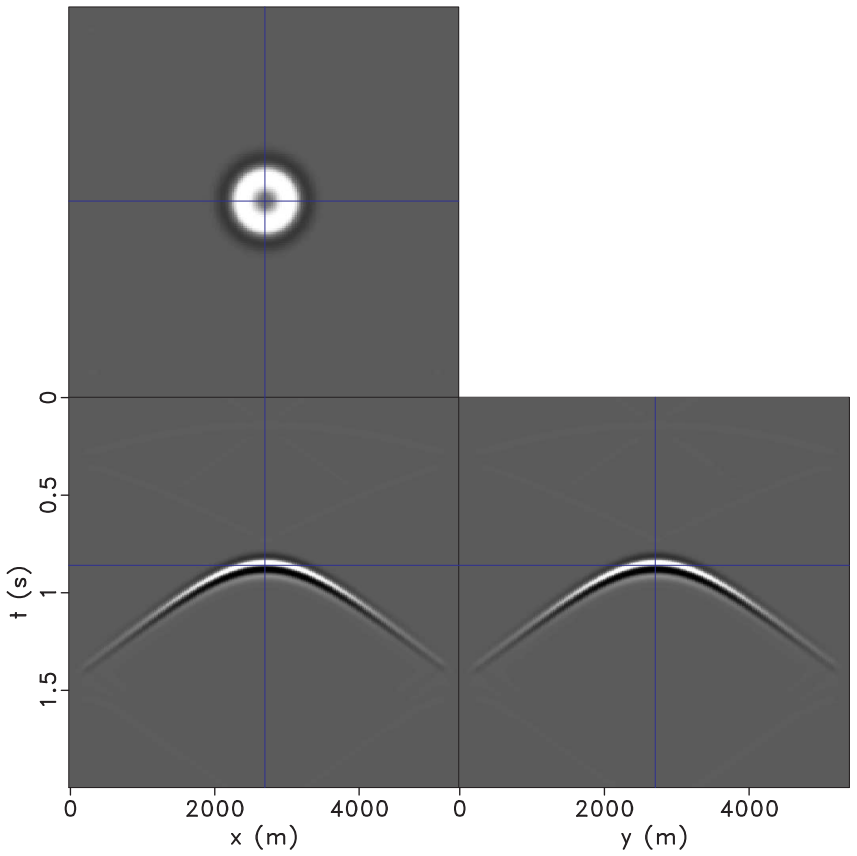

(a)

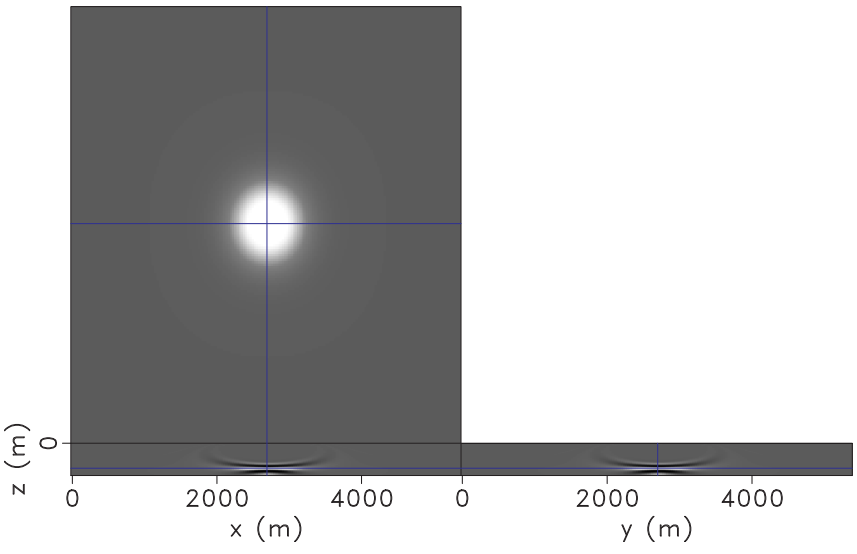

(b)

Figure 4.6. (a) Data for the one shot located at center of x-axis, (b) and image of horizontal reflector located at $z_r = 700$ m.

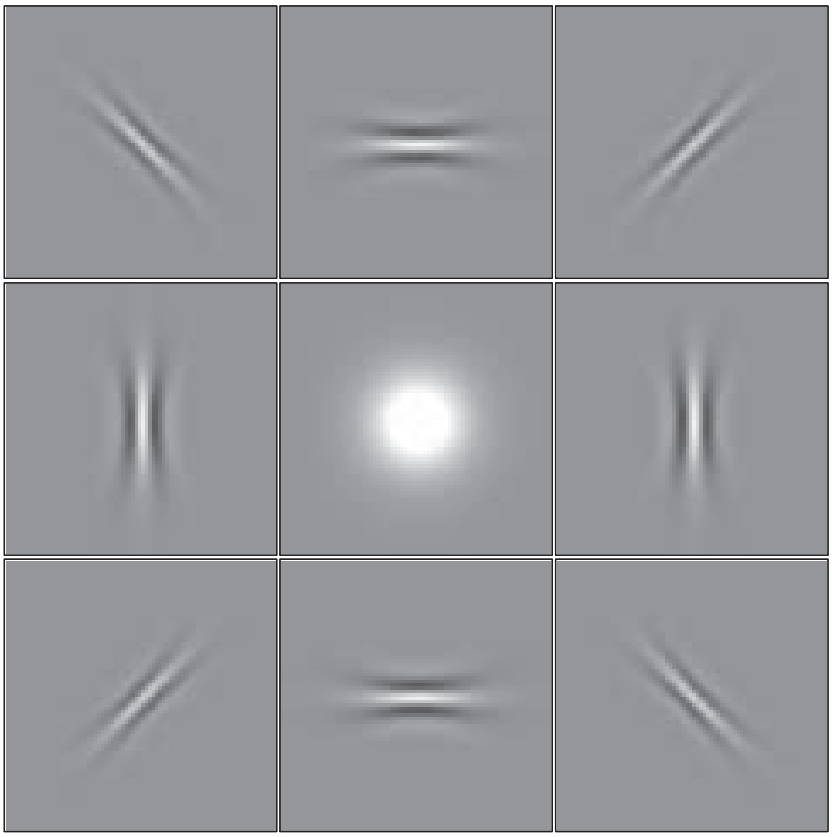

Figure 4.7. Space-lag domain common-image gathers: each individual plot is a lag gather for a different horizontal location over the reflector. In each Figure, the horizontal axis is λ_x and the vertical is λ_y. The gather in the center has the same horizontal location as the source. The gathers around the central one are located 300 m away from it in one or both horizontal directions.

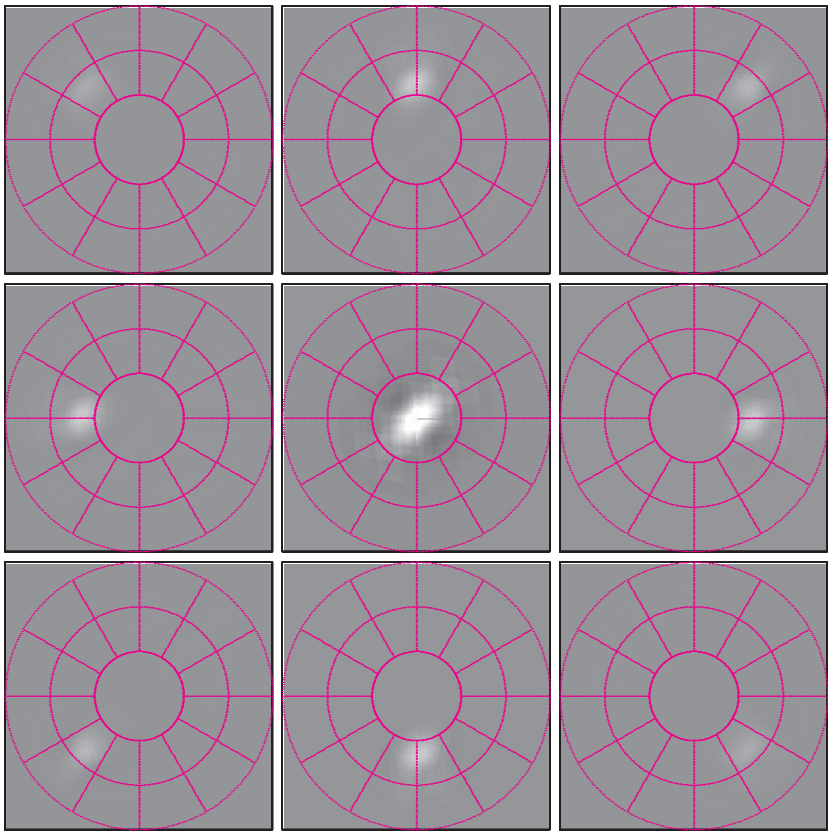

Figure 4.8. Angle-domain common-image gathers: each individual plot is the angle gather (CIG) obtained from the lag gathers in Figure 4.7. The gathers are displayed in a polar plot format.

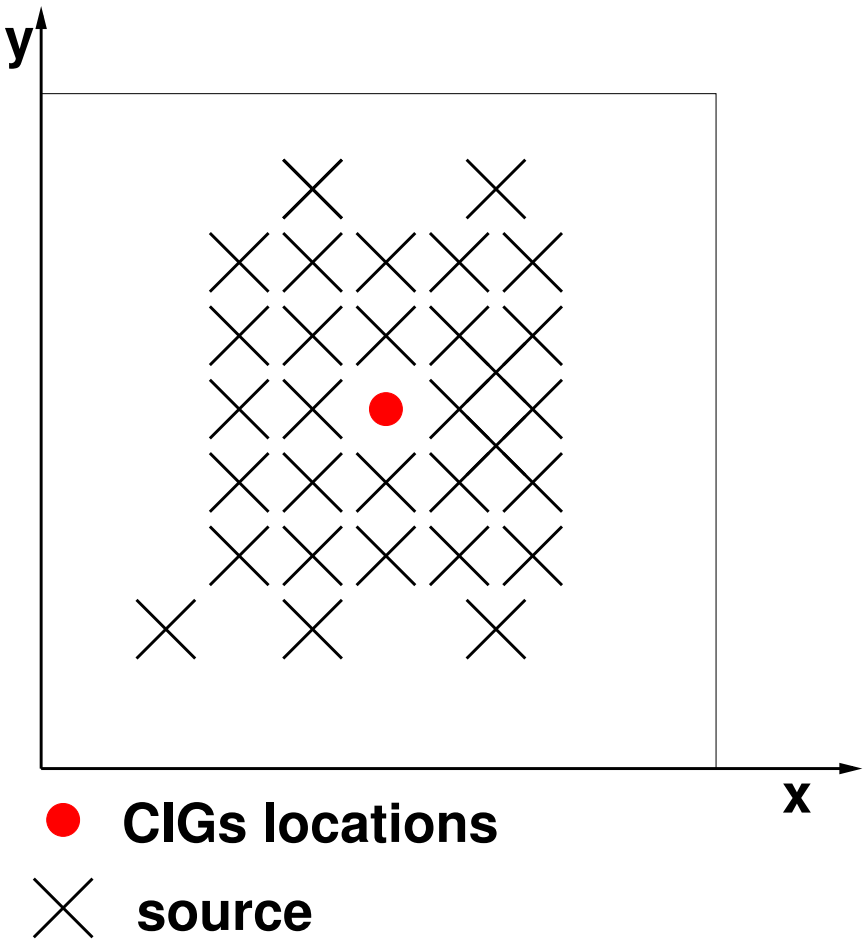

Figure 4.9. CIG locations. Each circle is a CIG location and the cross is the source location. There are 31 sources not uniformly spaced.

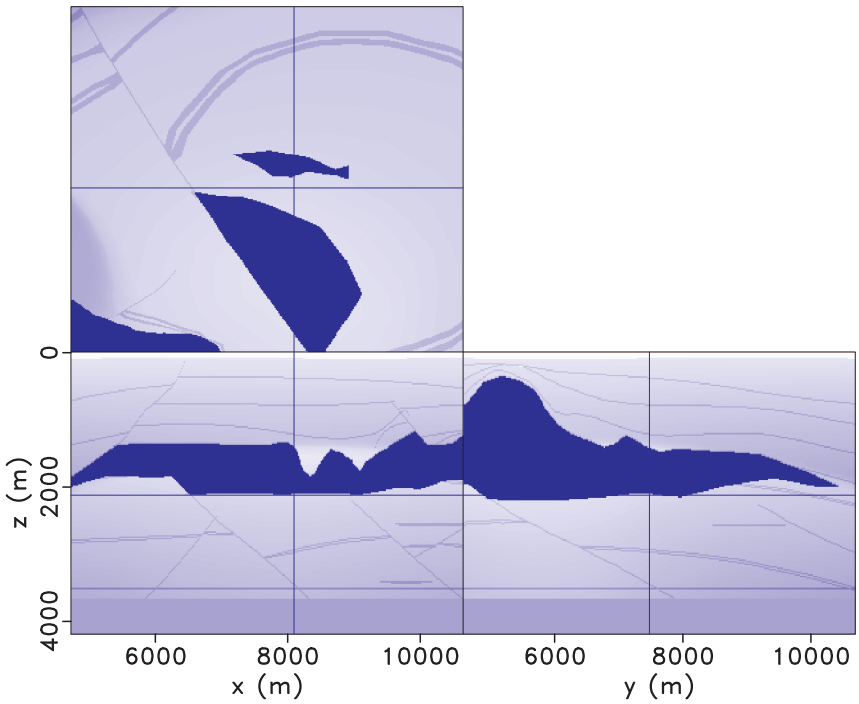

Figure 4.10. Velocity and reflectivity model for SEG/EAGE salt dome model.

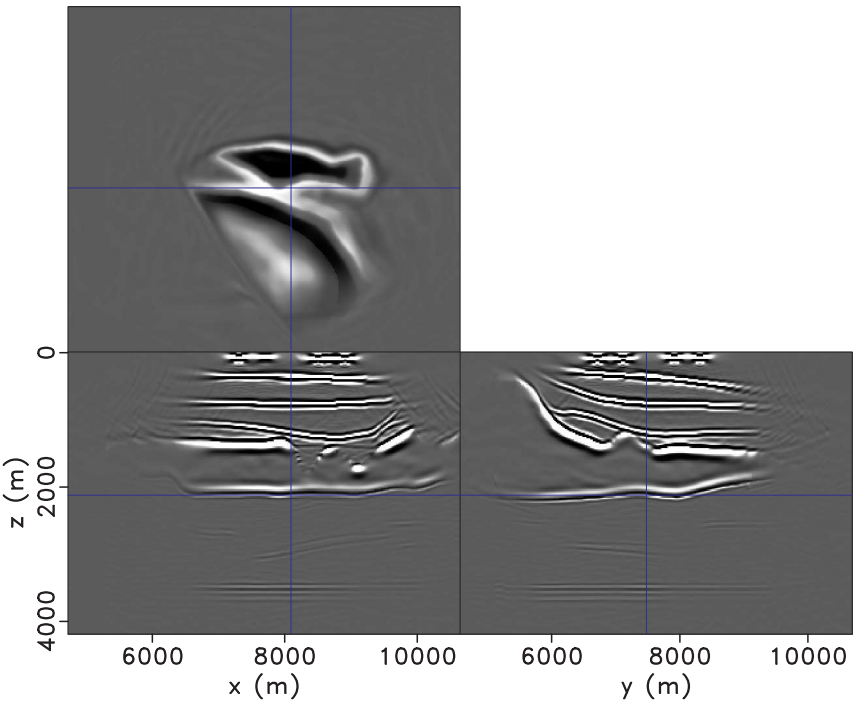

Figure 4.11. Migrated image for SEG/EAGE salt dome model.

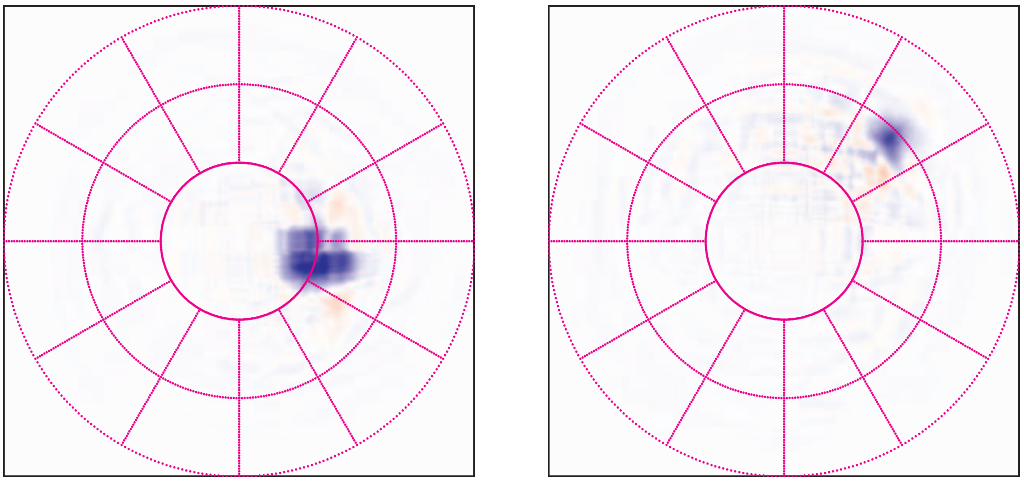

(a) (b)

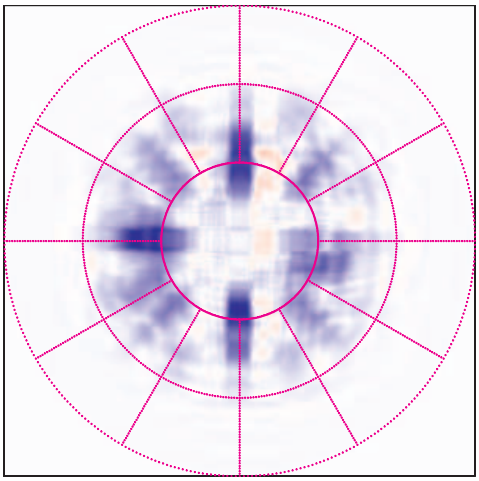

(c)

Figure 4.12. Polar representation of angle-domain common-image gathers for SEG/EAGE salt dome model. (a) and (b) are CIGs for two different individual shots for the same reflector location. (c) is the CIG for the same reflector location, but accounting for all the shots.

Chapter 5

Conclusions

One can extract information about reflection and azimuthal angle from the extended image $I(\boldsymbol{x}, \boldsymbol{\lambda})$ just by using simple relationships between ray parameter vectors. According to the analysis performed in this work, I conclude that when implementing the extended imaging condition one should use the smallest sample interval that is available for the space lags, which is the same sample interval as for the corresponding space coordinates. This is convenient since conventional implementations of the extended imaging condition keeps the space and space-lag sampling intervals the same. Using the angle information one can construct angle-dependent reflectivity. When constructing the angle gathers, the parameters to be chosen are the sample intervals for both reflection and azimuthal angles. They should be chosen in order to avoid aliasing the angle gathers.

I obtain reciprocal resolution/range relationships between lag and angle domains from the equations used to perform the lag to angle-domain mapping, together with the sampling parameters in both domains. The relationships show that the the angle-domain resolution is controlled by the range in the space-lag domain and that the angle-domain range is controlled by the resolution in the space-lag domain. In general, the angle that limits this range is proportional to the ratio between maximum depth wavenumber and maximum space-lag wavenumber. This angle limits the range of reflection angles for which energy focuses at the depth of the reflector in the angle gathers. In 3D, this angle range varies with the azimuthal angle. The largest wavenumbers of the lag gather limit the range of angles for which one can trust the amplitudes in the angle gather. This is particularly important if these angle gathers are being employed to perform amplitude versus angle analysis or migration velocity analysis.

References

Biondi, B., and Palacharla, G., 1996, 3-D prestack migration of common-azimuth data: Geophysics, 61, no. 06, 1822–1832.

Biondi, B., and Symes, W., 2004, Angle-domain common-image gathers for migration velocity analysis by wavefield-continuation imaging: Geophysics, 69, no. 5, 1283–1298.

Biondi, B., and Tisserant, T., 2004, 3D angle-domain common-image gathers for migration velocity analysis: Geophys. Prosp., 52, no. 6, 575–591.

Biondi, B., Tisserant, T., and Symes, W., 2003, Wavefield-continuation angle-domain common-image gathers for migration velocity analysis: Wavefield-continuation angle-domain common-image gathers for migration velocity analysis:, Soc. of Expl. Geophys., 73rd Ann. Internat. Mtg., 2104–2107.

Bleistein, N., Zhang, Y., Xu, S., Zhang, G., and Gray, S. H., 2005, Kirchhoff inversion in image point coordinates recast as source/receiver point processing: SEG Technical Program Expanded Abstracts, 24, no. 1, 1697–1700.

Brandsberg-Dahl, S., de Hoop, M. V., and Ursin, B., 1999, The sensitivity transform in the common scattering-angle/azimuth domain: The sensitivity transform in the common scattering-angle/azimuth domain:, Eur. Assn. Geosci. Eng., 61st Mtg., Session:4053.

Claerbout, J. F., 1971, Toward a unified theory of reflector mapping: Geophysics, 36, no. 03, 467–481.

Cockshott, I., and Jakubowicz, H., 1996, 3D migration using the Fourier finite difference method: 3D migration using the Fourier finite difference method:, Eur. Assn. Geosci. Eng., 58th Mtg., Session:P093.

Dobrin, M. B. M. B., 1988, Introduction to geophysical prospecting: , McGraw-Hill Book Co., 4th ed. edition.

Freire, R., and Stoffa, P. L., 1986, Migration using the 'Split-step Fourier' method: Migration using the 'Split-step Fourier' method:, Soc. of Expl. Geophys., 56th Ann. Internat. Mtg., Session:POS2.1.

Gazdag, J., and Sguazzero, P., 1985, Migration of seismic data by phase shift plus interpolation *in* **Gardner, G. H. F., Ed., Migration of seismic data:: Soc. of Expl. Geophys., 323–330.**

Gray, S. H., Etgen, J., Dellinger, J., and Whitmore, D., 2001, Seismic migration problems and solutions: Geophysics, 66, no. 5, 1622–1640.

Kessinger, W., 1992, Extended split-step Fourier migration: Extended split-step Fourier migration:, Soc. of Expl. Geophys., 62nd Ann. Internat. Mtg, 917–920.

LaDart, S., Lee, J., Shoshitaishvili, E., Etgen, J., and Michell, S., 2006, Wide azimuth tomography - is it necessary?: Wide azimuth tomography - is it necessary?:, Soc. of Expl. Geophys.

Michell, S., Shoshitaishvili, E., Chergotis, D., Sharp, J., and Etgen, J., 2006, Wide azimuth streamer imaging of mad dog; have we solved the subsalt imaging problem?: Wide azimuth streamer imaging of mad dog; have we solved the subsalt imaging problem?:, Soc. of Expl. Geophys.

Mosher, C., and Foster, D., 2000, Common angle imaging conditions for prestack depth migration: Common angle imaging conditions for prestack depth migration:, Soc. of Expl. Geophys., 70th Ann. Internat. Mtg, 830–833.

Nolan, C. J., and Symes, W. W., 1996, Imaging and coherency in complex structures: Imaging and coherency in complex structures:, Soc. of Expl. Geophys., 66th Ann. Internat. Mtg, 359–362.

Prucha, M., Biondi, B., and Symes, W., 1999, Angle-domain common image gathers by wave-equation migration: Angle-domain common image gathers by wave-equation migration:, Soc. of Expl. Geophys., 69th Ann. Internat. Mtg, 824–827.

Regone, C. J., 2006, A modeling approach to wide-azimuth design for subsalt imaging: The Leading Edge, 25, no. 12, 1467–1475.

Sava, P. C., and Fomel, S., 2003, Angle-domain common-image gathers by wavefield continuation methods: Geophysics, 68, no. 3, 1065–1074.

Sava, P., and Fomel, S., 2005, Coordinate-independent angle-gathers for wave equation migration: SEG Technical Program Expanded Abstracts, 24, no. 1, 2052–2055.

Sava, P., and Fomel, S., 2006, Time-shift imaging condition in seismic migration: Geophysics, 71, no. 6, S209–S217.

Shirui, W., Yun, L., and Xiangyu, G., 2006, Application of wide azimuth land 3d - a case history.: Application of wide azimuth land 3d - a case history.:, Soc. of Expl. Geophys.

Shoshitaishvili, E., Michell, S., Etgen, J., Chergotis, D., and Olson, E., 2006, Improving resolution of top salt complexities for subsalt imaging.: Improving resolution of top salt complexities for subsalt imaging.:, Soc. of Expl. Geophys.

Stoffa, P. L., Fokkema, J. T., de Luna Freire, R. M., and Kessinger, W. P., 1990, Split-step Fourier migration: Geophysics, 55, no. 04, 410–421.

Stolk, C. C., and Symes, W., 2002, Artifacts in Kirchhoff common image gathers: Artifacts in Kirchhoff common image gathers:, Soc. of Expl. Geophys., 72nd Ann. Internat. Mtg, 1129–1132.

Xu, S., Chauris, H., Lambare, G., and Noble, M. S., 1998, Common angle image gather: A new strategy for imaging complex media: Common angle image gather: A new strategy for imaging complex media:, Soc. of Expl. Geophys., 68th Ann. Internat. Mtg, 1538–1541.

Appendix A

Angle decomposition equations

This appendix closely follows the derivation from Sava & Fomel (2005).

The image obtained from the space lag (extended) imaging condition (equation2.2) is a function of space $\boldsymbol{x}$ and space lags $\boldsymbol{\lambda}$. I define the local source and receiver coordinates $\boldsymbol{s} = (s_x, s_y, s_z)$ and $\boldsymbol{r} = (r_x, r_y, r_z)$, respectively, in terms of $\boldsymbol{x}$ and $\boldsymbol{\lambda}$ (Figure 2.1),

$$\boldsymbol{s} = \boldsymbol{x} - \boldsymbol{\lambda}\,, \tag{A.1}$$

$$\boldsymbol{r} = \boldsymbol{x} + \boldsymbol{\lambda}\,. \tag{A.2}$$

The two-way traveltime $t = t\,(\boldsymbol{x}, \boldsymbol{\lambda})$ from a source to a receiver location is a function of $\boldsymbol{x}$ and $\boldsymbol{\lambda}$. The traveltime can be regarded as function of $\boldsymbol{s}$ and $\boldsymbol{r}$, $t = t\left(\dfrac{\boldsymbol{r}+\boldsymbol{s}}{2}, \dfrac{\boldsymbol{r}-\boldsymbol{s}}{2}\right)$. Changes in the traveltime with respect to change in x, y and z are, respectively,

$$\begin{aligned}\frac{\partial t}{\partial x} &= \frac{\partial t}{\partial r_x}\frac{\partial r_x}{\partial x} + \frac{\partial t}{\partial s_x}\frac{\partial s_x}{\partial x} \\ &= \frac{\partial t}{\partial r_x} + \frac{\partial t}{\partial s_x}\,,\end{aligned} \tag{A.3}$$

and

$$\begin{aligned}\frac{\partial t}{\partial y} &= \frac{\partial t}{\partial r_y}\frac{\partial r_y}{\partial y} + \frac{\partial t}{\partial s_y}\frac{\partial s_y}{\partial y} \\ &= \frac{\partial t}{\partial r_y} + \frac{\partial t}{\partial s_y}\,,\end{aligned} \tag{A.4}$$

and

$$\begin{aligned}\frac{\partial t}{\partial z} &= \frac{\partial t}{\partial r_z}\frac{\partial r_z}{\partial z} + \frac{\partial t}{\partial s_z}\frac{\partial s_z}{\partial z} \\ &= \frac{\partial t}{\partial r_z} + \frac{\partial t}{\partial s_z}\,,\end{aligned} \tag{A.5}$$

Similarly, changes in the traveltime with respect to λ_x, λ_y and λ_z are, respectively,

$$\begin{aligned}\frac{\partial t}{\partial \lambda_x} &= \frac{\partial t}{\partial r_x}\frac{\partial r_x}{\partial \lambda_x} + \frac{\partial t}{\partial s_x}\frac{\partial s_x}{\partial \lambda_x} \\ &= \frac{\partial t}{\partial r_x} - \frac{\partial t}{\partial s_x}\,.\end{aligned} \tag{A.6}$$

and

$$\begin{aligned}\frac{\partial t}{\partial \lambda_y} &= \frac{\partial t}{\partial r_y}\frac{\partial r_y}{\partial \lambda_y} + \frac{\partial t}{\partial s_y}\frac{\partial s_y}{\partial \lambda_y} \\ &= \frac{\partial t}{\partial r_y} - \frac{\partial t}{\partial s_y}\,, \end{aligned} \tag{A.7}$$

and

$$\begin{aligned}\frac{\partial t}{\partial \lambda_z} &= \frac{\partial t}{\partial r_z}\frac{\partial r_z}{\partial \lambda_z} + \frac{\partial t}{\partial s_z}\frac{\partial s_z}{\partial \lambda_z} \\ &= \frac{\partial t}{\partial r_z} - \frac{\partial t}{\partial s_z}\,, \end{aligned} \tag{A.8}$$

Since $\boldsymbol{p} = \nabla t$, I can relate the wavenumber vectors as

$$\boldsymbol{p_x} = \boldsymbol{p_r} + \boldsymbol{p_s}\,, \tag{A.9}$$

$$\boldsymbol{p_\lambda} = \boldsymbol{p_r} - \boldsymbol{p_s}\,. \tag{A.10}$$

where $\boldsymbol{p_x}$, $\boldsymbol{p_\lambda}$, $\boldsymbol{p_s}$, and $\boldsymbol{p_r}$ are the wavenumber vectors relative to $\boldsymbol{x}$, $\boldsymbol{\lambda}$, $\boldsymbol{s}$, and $\boldsymbol{r}$, respectively.

If $\boldsymbol{k_x}$ and $\boldsymbol{k_\lambda}$ are the space and space-lag wavenumber vectors, respectively, we have

$$\boldsymbol{p_x} = \frac{\boldsymbol{k_x}}{\omega}\,, \tag{A.11}$$

$$\boldsymbol{p_\lambda} = \frac{\boldsymbol{k_\lambda}}{\omega}\,. \tag{A.12}$$

Using the fact that $\boldsymbol{p_x}$ and $\boldsymbol{p_\lambda}$ are orthogonal by definition, we obtain an expression for the reflection angle θ

$$|\tan(\theta)| = \frac{|\boldsymbol{p_\lambda}|}{|\boldsymbol{p_x}|} = \frac{|\boldsymbol{k_\lambda}|}{|\boldsymbol{k_x}|} \tag{A.13}$$

$$= \frac{\sqrt{k_{\lambda_x}^2 + k_{\lambda_y}^2 + k_{\lambda_z}^2}}{\sqrt{k_x^2 + k_y^2 + k_z^2}}\,. \tag{A.14}$$

I can define the azimuthal angle as the angle between any vector that rotates along with the reflection plane and an arbitrary direction. The vector $\boldsymbol{p_x} \times \boldsymbol{p_\lambda}$ is contained in the reflecting plane and rotates 360° with the reflection plane. Let ν be an arbitrary direction, then the azimuthal angle between $\boldsymbol{p_x} \times \boldsymbol{p_\lambda}$ and ν is given by

$$\cos\phi = \frac{(\nu)\cdot(\boldsymbol{p_x} \times \boldsymbol{p_\lambda})}{|\nu||\boldsymbol{p_x} \times \boldsymbol{p_\lambda}|}\,. \tag{A.15}$$

Here, I choose to define the x-axis (in-line) direction as the azimuthal reference direction $\nu = (1, 0, 0)$, and the azimuthal angle as the angle between the line of intersection line between the reflection plane and the horizontal x-y plane and the x-axis. One advantage of this choice of reference is that it allows one to study local media property

variations in relation to the same direction. One disadvantage of this choice is that this definition breakes down for vertical reflectors because the intersection between all possible reflection planes, at a fixed image point location, and the horizontal plane all have the same direction.

Let vector $\boldsymbol{d}$ be the cross-product of the vectors $\boldsymbol{p_\lambda}$ and $\boldsymbol{p_x}$,

$$\begin{aligned} \boldsymbol{d} &= \boldsymbol{p_\lambda} \times \boldsymbol{p_x} && \text{(A.16)} \\ &= (p_{\lambda_y} p_z - p_{\lambda_z} p_y, p_{\lambda_z} p_x - p_{\lambda_x} p_z, p_{\lambda_x} p_y y - p_{\lambda_y} p_x) \; . && \text{(A.17)} \end{aligned}$$

As indicated earlier, $\boldsymbol{d}$ is orthogonal to the reflection plane and it is contained in the reflecting plane. As the reflection plane rotates, the vector $\boldsymbol{d}$ also rotates, so we can associate the orientation of $\boldsymbol{d}$ with the orientation of the reflection plane. Let $\boldsymbol{d}_h = (d_x, d_y, 0)$ be the horizontal projection of $\boldsymbol{d}$ in the x-y plane. I define the azimuthal angle ϕ as the angle between $\boldsymbol{d}$ and the in-line direction, so

$$\cos\phi = \frac{k_{\lambda_y} k_z - k_{\lambda_z} k_y}{\sqrt{(k_{\lambda_y} k_z - k_{\lambda_z} k_y)^2 + (k_{\lambda_z} k_x - k_{\lambda_x} k_z)^2}} \; . \tag{A.18}$$

Since $\boldsymbol{k_\lambda}$ and $\boldsymbol{k_x}$ are orthogonal to each other

$$\boldsymbol{k_\lambda} \cdot \boldsymbol{k_x} = k_{\lambda_x} k_x + k_{\lambda_y} k_y + k_{\lambda_z} k_z = 0 \; , \tag{A.19}$$

and

$$k_{\lambda_z} = \frac{-k_{\lambda_x} k_x - k_{\lambda_y} k_y}{k_z} \; . \tag{A.20}$$

Thus, I can eliminate k_{λ_z} from equations A.14 and A.18 and rewrite these equations as

$$\tan\theta = \frac{\sqrt{(k_{\lambda_x}^2 + k_{\lambda_y}^2) k_z^2 + (-k_x k_{\lambda_x} - k_y k_{\lambda_y})^2}}{\sqrt{k_z^2 (k_x^2 + k_y^2 + k_z^2)}} \; , \tag{A.21}$$

and

$$\cos\phi = \frac{k_z^2 k_{\lambda_y} + k_x k_y k_{\lambda_x} + k_y^2 k_{\lambda_y}}{\sqrt{(k_z^2 k_{\lambda_y} + k_x k_y k_{\lambda_x} + k_y^2 k_{\lambda_y})^2 + (-k_x^2 k_{\lambda_x} - k_y k_x k_{\lambda_y} - k_{\lambda_x} k_z^2)^2}} \; . \tag{A.22}$$